SYNTHETIC APERTURE FOCUSING TECHNIQUE USING A VIRTUAL TRANSDUCER ELEMENT SOURCE

BY

CATHERINE ANN HILLSLEY FRAZIER

B.S.E.E., University of Maryland at College Park, 1994

THESIS

Submitted in partial fulfillment of the requirements
for the degree of Master of Science in Electrical Engineering
in the Graduate College of the
University of Illinois at Urbana-Champaign, 1996

Urbana, Illinois

UNIVERSITY OF ILLINOIS AT URBANA-CHAMPAIGN

THE GRADUATE COLLEGE

MAY 1996

WE HEREBY RECOMMEND THAT THE THESIS BY

CATHERINE ANN HILLSLEY FRAZIER

ENTITLED SYNTHETIC APERTURE FOCUSING TECHNIQUE USING A VIRTUAL

TRANSDUCER ELEMENT SOURCE

BE ACCEPTED IN PARTIAL FULFILLMENT OF THE REQUIREMENTS FOR

THE DEGREE OF MASTER OF SCIENCE

W. D'Brien

Director of Thesis Research

D. M. Long

Head of Department

Committee on Final Examination†

Chairperson

† Required for doctor's degree but not for master's.

O-517

ACKNOWLEDGEMENTS

I would like to thank my advisor Professor William O'Brien Jr., for his time and guidance throughout this study. I have benefitted greatly from his knowledge and experience. Professor O'Brien has an ability to bring varied and interesting projects into the laboratory, for which I am grateful. I would also like to thank the students of the Bioacoustics Research Laboratory for their discussions and interest in my work.

Finally, I must thank my family for their support in this and many other endeavors. I am fortunate to have such a solid foundation.

DEDICATION

This thesis is dedicated to my growing family, for encouragement and support, but above all for pleasant distractions.

TABLE OF CONTENTS

LIST OF TABLES

LIST OF FIGURES

CHAPTER 1

INTRODUCTION

The development of ultrasound for use in imaging systems began in the 1940s when the techniques that had been developed for radar systems were being applied to sonar systems for underwater imaging. With the advent of grayscale displays in the 1970s, ultrasonic imaging became widely used [1]. Ultrasound has been applied to medical diagnostic imaging, nondestructive evaluation, and subsurface imaging. Recent research in ultrasonic imaging has focused on improving resolution or signal to noise ratio (SNR), simplifying the construction of images, or applying the techniques to new imaging situations. In the medical community, ultrasound is being developed for intervascular, dermatologic, ocular or other diagnostic imaging [2]–[4]. In subsurface imaging, synthetic aperture techniques are being used to discern features and buried objects rather than to simply determine properties of the underground environment [5]. With the new applications and the need for improved images come expansions in the range of frequencies used, advances in transducer fabrication, and developments in imaging configurations and data collection.

Currently ultrasonic imaging is performed with one of two data collection configurations: conventional brightness mode (B-mode) imaging, or array imaging. In conventional B-mode imaging, a single mechanically focused transducer is translated to collect data. In array imaging, several small transducer elements are used to collect data, and the received signals are focused using computer processing. In this thesis, a method is examined for improving the resolution of ultrasonic images through the combination of conventional B-mode and synthetic aperture techniques. The

possibility of applying techniques developed for an actual small element to a virtual source which is the focal spot of a focused transducer is explored. The virtual source technique is tested through the processing of experimentally collected data. The images are examined for resolution, SNR, and contrast, and these results are compared to reported results for images created with transducer arrays. A virtual source is found to behave similarly to an actual transducer element in response to synthetic aperture focusing techniques. Therefore, synthetic aperture techniques can be applied to the region of an image beyond the focus of a transducer to improve the resolution. It is hoped that the results developed in this thesis will apply to the general problem of imaging targets hidden from view without disturbing their environment.

The remainder of this introduction gives some background information for the study of this problem. A brief summary of the development of synthetic aperture imaging and ultrasonic medical diagnostic imaging is followed by a general description of conventional B-mode and current synthetic aperture imaging techniques. Finally, the organization of the thesis is given.

1.1 Ultrasonic Imaging Techniques

In the early development of ultrasonic imaging, B-mode images were created with unfocused transducers by scanning them along a line. For viewing structures within the body, the unfocused transducers did not have acceptable resolution at any point along the beam. Mechanically focused beams were developed to replace the unfocused beams; however, it was recognized that the resolution of the image was only improved over a small depth of field, and everywhere else the resolution had actually become worse due to the spreading of the beam. In 1974, Burckhardt, Grandchamp, and Hoffmann [6] proposed the first synthetic aperture system for medical use. Their method was a combination of synthetic aperture sonar techniques and holography.

Since then, synthetic aperture techniques have been among those used in medical ultrasound to produce images for diagnosis.

The highest quality ultrasound images are produced using a more complicated electronically focused technique called phased array imaging [7]. In this case, the transducer is an array of small elements that are all excited simultaneously. This configuration differs from a synthetic aperture in which the elements are excited in sequence. The signals from individual elements are delayed in various ways to steer and focus the beam. The images are high quality because phased array imaging overcomes the limitations of both fixed focus imaging and synthetic aperture imaging. Briefly, fixed focus B-mode imaging produces images with good resolution only in the area near the focus of the transducer. In phased array imaging, because the beam is focused at many depths, the whole image is in focus. Synthetic aperture imaging also allows the whole image to be in focus, but resulting images suffer from a low SNR because the individual element does not output much power. Phased arrays excite all the transducer elements at once; therefore, more power is output. Although the phased array images are good, the hardware or processing necessary to obtain the images can be too complex for some applications.

A combination of the current imaging techniques is proposed to produce a focused image with an acceptable SNR. The new technique uses the focus of a mechanically focused transducer as a virtual source for a synthetic aperture imaging technique. In the final image, the region near the focus would be processed according to conventional B-mode imaging, and the deeper parts of the image would be focused through synthetic aperture processing.

1.1.1 B-mode imaging

B-mode images are produced in the following way. The transducer transmits a pulse. As the energy from the pulse is reflected by structures within the target, the

same transducer receives the reflections. The time until the pulse is received indicates how far away the structure is from the transducer. The amplitude of the reflection indicates how different the properties of the structure are from the properties of the medium. A reflected rf signal is called an A-line. After receiving the signal, the transducer is moved to the next position. The next position should be far enough away that the two received A-lines can be considered independent. The image is created by filtering the received signals with an envelope detector and displaying the filtered signals side by side. One axis of the final image represents the position of the transducer during the lateral scan, the other axis represents the depth into the medium, and the brightness of the pixel represents the strength of the reflection. The lateral motion of the transducer may be replaced by steering the transducer beam to different angles to produce what is known as a sector scan.

Ideally, the transmitted beam would have infinitesimal width, so that the position of the reflector would be exactly known from the position of the transducer and the time until the reflection was received. The ability to distinguish between two points close together at the same depth is called lateral resolution. Unfortunately, the ideal beam is impossible to achieve. Instead, conventional B-mode imaging employs a focused transducer, which has a narrow beam over a range of distances that includes the focus. The region where the beam is considered narrow is called the depth of focus. At the focal point the best lateral resolution for the transducer is achieved. For the region around the focus described by the depth of focus, the lateral resolution is acceptable.

In the ideal case, the transmitted pulse would also have infinite bandwidth to achieve good axial resolution. Axial resolution is the ability to distinguish between two targets located at the same lateral position and close in range. A pulse with infinite bandwidth has an infinitesimal time duration. Again, this ideal is impossible to achieve. Instead short pulses with broad frequency support are used.

The received signals are processed before they are displayed as an image. First, the signals are bandpass filtered to remove noise. Next, they are envelope detected, a process that removes the carrier frequency and rectifies the signal. The envelope detected signal is amplified with a variable gain amplifier in a process referred to as time-gain compensation. The amplifier gain increases with the depth of the returned signal to compensate for the effects of attenuation in the medium. Then the data are logarithmically compressed so that the entire dynamic range can be displayed. Finally, the A-lines are displayed side by side using grayscale values to represent the amplitude of the signal at given points.

1.1.2 Synthetic aperture imaging

In various fields, synthetic aperture imaging has been described in terms of the Doppler effect, a matched filtering operation, and as the focusing of an array [8]. Traditionally, the ultrasound community has used the beam focusing description, which is presented here.

In the absence of some processing, the lateral resolution achieved at a given depth is equal to the width of the beam at that depth. Therefore, focusing refers to creating a narrow beam at a given location. After synthetic aperture processing, an A-line will be the sum of the received signals from several array elements. To create the focus, the received signals from the location of the desired focus must add coherently. In other words, the individual pulses must arrive at the point with the same phase, or equivalently, making the pulses arrive at the same time. The signals from different elements have to travel different distances to the desired focal point. Therefore, making the pulses add at the focal point involves delaying the elements with the shorter pathlengths appropriately. The calculation of these delays is presented in detail in the next chapter. After the A-lines have been created by summing the

delayed signals from several of the elements, the processing continues in the same manner as for B-mode imaging.

The goal of this imaging technique is to synthesize the beam pattern of a large element. The small element transducer can be considered a sample of the large aperture. The span of the elements included in the sum determines the size of the synthesized large element, while the spacing between the samples determines the sampling rate. A larger synthesized aperture can achieve a more highly focused system, so it is desirable to use a large number of elements in the sum. When attempting to focus at a given point, only those elements whose beams encompass that point should be used in the sum. Including additional elements reduces the SNR because they contribute only to the noise. The number of elements used is therefore limited by their beam spread. Since it is desirable to use a large number of elements, it follows that the elements should have a large beam spread. The beam spread is inversely proportional to the size of the transducer; therefore, the elements should be as small as possible. However, small sources are inefficient radiators, transmitting less energy into the medium. This again results in a lower SNR. A balance must be achieved between the beam spread and the power output of the elements used.

There are also restrictions on the spacing of the elements. If the elements are spaced too far apart, the coherent sum of the received signals will achieve a maximum, not only at the desired focal point but also at other angles. These other maxima, known as grating lobes, degrade the image quality. They can be eliminated by placing the array elements closer together; however, there are limitations on how close together elements can be placed, given the required physical dimensions of the elements and the desire to keep the amount of data collected as small as possible. These are the tradeoffs that must be balanced in designing a synthetic aperture imaging system.

1.2 Recent Improvements to Synthetic Aperture Images

As mentioned above, phased arrays produce the best quality images because the beam can be focused at multiple depths, and a large number of elements transmit and receive pulses at once, increasing the SNR. However, phased array images also require the most complex data collection and processing, because focusing the beam at several depths on transmit requires several transmit pulses to collect one received A-line. The data collection in synthetic aperture approaches is much simpler. Therefore, recent work has been done to improve the quality of these images.

One problem with array imaging is that if the elements of the array are not packed together closely enough, grating lobes will appear and degrade the quality of the image. The formation of grating lobes is discussed in more detail in Chapter 2. Grating lobes cannot always be eliminated by placing the array elements closer together, due to practical considerations of building the array. The elements must be separated by some distance to prevent cross-talk between them. Two groups have proposed a method to reduce grating lobes through a modified data collection scheme, which one group calls interlacing [9] and [10]. Effectively the missing samples are replaced by separating the transmit and receive elements. Typical data collection involves transmitting a wave from one element, receiving the echo at the same element, and then repeating the process with the remaining elements of the array. In the new scheme, the data collection proceeds as follows: transmit from element 1, receive at element 1; transmit at element 1, receive at element 2; transmit at element 2, receive at element 2; transmit at element 2, receive at element 3, etc. By separating the transmit and receive elements, the researchers create a virtual element between the existing ones.

In 1994, J. T. Ylitalo and H. Ermert [11] proposed a method to increase the dynamic range of images produced using synthetic aperture processing. The method

involves focusing to various degrees the beam of the individual element. The focusing is achieved by increasing the number of elements that transmit at once. Essentially the method increases the dynamic range of an image by increasing the power output to the medium. However, by making the individual beams more narrow, lateral resolution has been sacrificed. Their work centers around finding an acceptable trade off between the dynamic range and the lateral resolution.

In 1995, M. Karaman, P.-C. Li, and M. O'Donnell [7] showed that the improvement in dynamic range can be achieved without increasing the lateral resolution. In their method, multiple elements are used for transmit. By delaying the individual elements appropriately, the beam produced can be made to simulate the beam pattern of a single small element. These delays are essentially the opposite of the delays used to focus an array. Firing several elements at once, they collected rf data. Then they used the usual synthetic aperture techniques to produce the image.

The research discussed above concentrates on array imaging because it is so common in medical ultrasonic imaging. In other imaging situations, it may be more practical to use a single transducer. The research presented in this thesis uses a single focused transducer for data collection.

1.3 Organization of This Thesis

The following chapters discuss the theoretical development and experimental validation for using the focus of a transducer as a virtual source. Chapter 2 presents the theory behind the concepts to be tested, such as how to reduce sidelobes, how to eliminate grating lobes, and how to accomplish beamforming. In Chapter 3, experimental results are presented to confirm the predictions of the theory using data collected from a tissue mimicking phantom. Finally, Chapter 4 presents the conclusions of this thesis and offers suggestions for future work.

CHAPTER 2

THEORETICAL DEVELOPMENT

Synthetic aperture imaging has been used in ultrasonic imaging for many years. In ultrasound literature, the technique is usually referred to as the synthetic aperture focusing technique (SAFT), in keeping with the viewpoint that the processing operates to create a focused beam from the individual elements of an array. Some of the theory that has been developed for SAFT and improving the images is presented here. This chapter begins with the development of a model for the virtual source. Then the basic delay and sum SAFT processing is presented, followed by discussions of various problems with the basic procedure and some ways of solving those problems.

2.1 Beam Pattern of a Virtual Source

Before any synthetic aperture processing can begin, the beam pattern of the source must be known, at least to the extent of knowing the half angle of beam spreading. The beam spread is important for determining the number of elements to include in the sum. As stated in the introduction, the signal to noise ratio (SNR) is maximized by including in the sum all the elements whose beams encompass the given focal point, and excluding all other elements.

The beam spread of a source is determined by the geometry of the source and the wavelength of sound in the medium. Therefore, the geometry of the virtual source must be modeled. One simple approach is to model the focus as a point source, since the focal spot of the transducer is supposed to be very small. This is the approach taken by C. Passman and H. Ermert [12] in their study using very highly

focused transducers. However, the focus of a transducer is generally not smaller than a wavelength. The focal diameter is in fact described by $d \approx \frac{F}{D}\lambda$ where d is the focal diameter, F is the focal distance, D is the diameter of the source, and λ is the wavelength in the medium. The transducer beam with these parameters labelled is shown in Figure 2.1. The ratio of F to d, referred to as the f-number of the transducer, is an indication of the strength of the transducer's focus. The f-number is rarely less than one. Therefore, the criterion for a source to be considered small, $ka \ll 1$, cannot be met. In that expression, k is the wavenumber equal to $\frac{2\pi}{\lambda}$, and a is the radius of the virtual source equal to $\frac{d}{2}$ in which d has been shown above to be greater than λ.

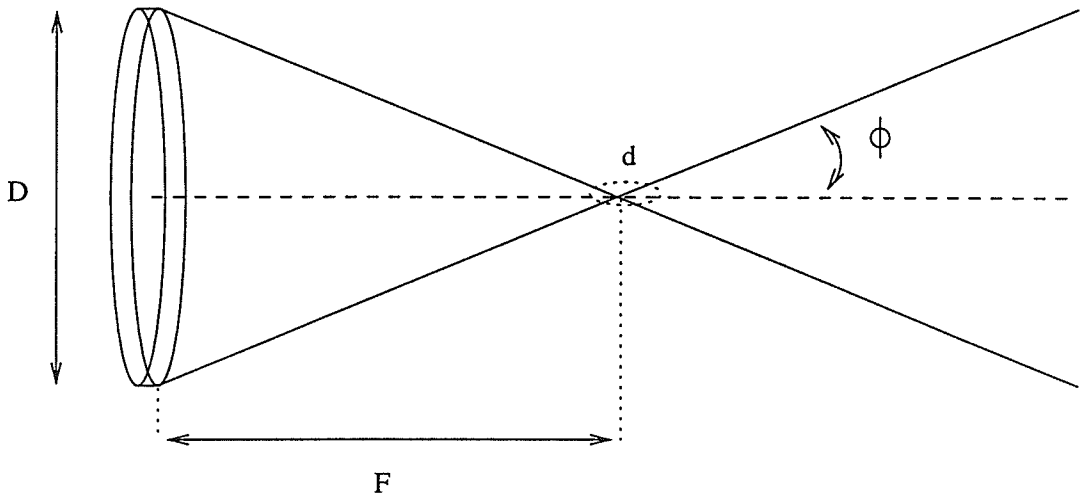

Figure 2.1: Parameters that describe transducer beam

The virtual source cannot be taken as arbitrarily small, but its size can be estimated as the actual size of the focal spot. Then the degree of beam spreading beyond the source measured between nulls is approximated by the expression

$$\sin(\phi_n) \approx \frac{\lambda}{d} \tag{2.1}$$

in which ϕ_n is the half angle of beam spreading measured between nulls, d is the diameter of the virtual source, and λ is the wavelength. The degree of spreading

measured between 6 dB points is estimated from the size of the source using the following expression.

$$\sin(\phi_{6dB}) = \frac{0.514c}{fD} \tag{2.2}$$

where ϕ_{6dB} is the half angle of beam spreading, c is the speed of sound in the medium, f is the frequency, and d is the diameter of the virtual source. Given a focal spot with diameter 300 μm, the degree of spreading would be 19.5 degrees between nulls and 9.74 degrees between 6 dB points.

Another method for modelling the virtual source matches the size and shape of the virtual transducer to what is known about a focused beam pattern. In other words, instead of finding the beam pattern from what is known of the dimensions of the focal spot, the size of the virtual source is determined from the measured degree of spreading. The virtual source is not focused, and it has cylindrical symmetry like the focused transducer that generated it; therefore, the source should be modelled by a plane circular piston. The initial beam spread after the focus will look approximately like the reverse of the beam pattern up to the focus, and the degree of spreading is approximately equal to the degree of focusing before the spot. The half angle at which the beam spreads can then be approximated by $\phi = \sin^{-1}\frac{D}{2F}$, where ϕ is the half angle of spreading measured between nulls, F is the focal distance, and D is the diameter of the focused transducer, as shown previously in Figure 2.1, page 10. By this formulation, the virtual source used in this experiment has a half angle of beam spread 19.5 degrees. This virtual source would be a plane circular piston with diameter 300 μm calculated from Equation (2.1).

In synthetic aperture imaging, it is desirable to have the transducer element as small as possible in order to obtain good resolution. This can be seen intuitively by considering that, in general, in order to obtain good resolution, the aperture should be as large as possible. When imaging with synthetic aperture techniques, the received signals from several elements are added together. Only those elements whose beam

patterns include the desired focal point should be included in the sum, or the SNR will be decreased. If each individual element has a wide beam, then more of them will encompass the desired point. Therefore, the returned signals from more elements can be included in the sum, and the sampled aperture, which includes more elements, will be larger. Of course, the individual elements should not be made too small. As acoustic sources decrease in size they become more inefficient radiators, and less power will be radiated into the medium for use in imaging.

2.2 Delay and Sum Beamforming

Once the beam pattern has been characterized, the image creation can occur. The delay and sum beamforming approach is the most intuitive of the focusing approaches. A portion of the array is shown in Figure 2.2. It is desired to focus at a point P that is located in the far field of the individual elements and in the transition region of the subaperture of the array. The field from the subaperture will be focused at P if the pulses from all the elements arrive simultaneously at P. This is achieved by advancing the signals from the elements farther away from the center of the subaperture and summing the received signals from all the elements in the subaperture. Simply using the Pythagorean theorem to find the pathlength for an element i, the amount of the advance should be

$$\Delta t_i = \frac{z - \sqrt{z^2 + (id)^2}}{c} \tag{2.3}$$

where t is time, z is the axial distance, i is the element number with zero assigned to the center element, d is now the interelement distance, and c is the speed of sound. Rearranging Equation (2.3) gives

$$\Delta t_i = \frac{z}{c}\left(1 - \sqrt{1 + \frac{(id)^2}{z^2}}\right) \tag{2.4}$$

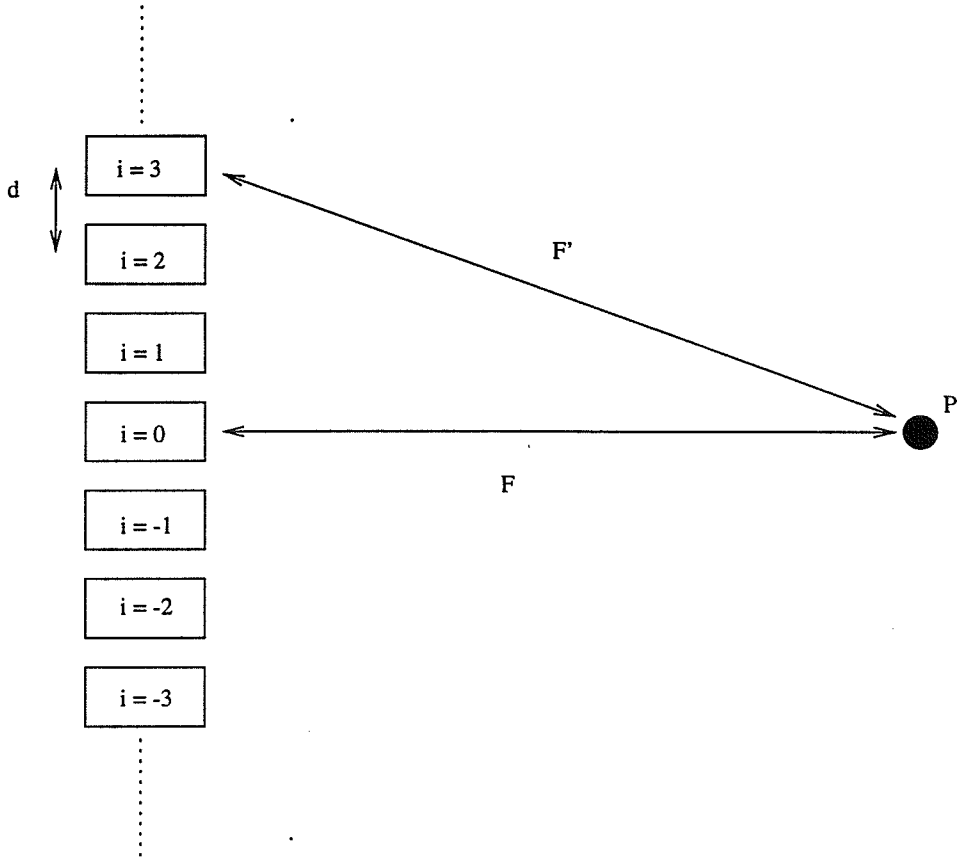

Figure 2.2: Geometric focusing

If the extent of the subaperture of the array is much smaller than the distance to the point P, Δt can be approximated by using the binomial theorem as

$$\Delta t_i = -\frac{(id)^2}{2zc} \tag{2.5}$$

This approximation is not appropriate for the images in this thesis since the extent of the subaperture is generally comparable to the distance to the focus. The approximation can be made when the length of the synthesized aperture is much smaller than the distance to the focal point which corresponds to a large f-number. However, to create a small focal spot, a small f-number is desired because the diameter of the focal spot can be estimated as the product of the f-number and the wavelength.

The delays calculated in Equation (2.4) are actually advances in time. Rather than advancing the signals, a constant delay can be added to each element so that the signals are all delayed. Also, from Equation (2.4) it is clear that the delays depend on the range of the desired focus. Thus, to create an image that is in focus over the whole axial range, the delays must be recalculated for many depths. The depth for which a specific set of delays is applicable is referred to as the depth of focus.

2.3 Lowering Sidelobes

The basic delay and sum beamforming technique results in a beam pattern with relatively large sidelobes that degrade the quality of the image. A received rf echo is the sum of all the reflections from targets at different depths with the same lateral position. Ideally, each reflection would be from a single point, but if the beam is wide, the reflection is actually an integral of the reflections from all targets within the area intercepted by the beam. A larger main beam results in poor resolution. If large sidelobes are present, the total reflection also includes contributions from targets illuminated by these lobes. In this case, targets with different lateral positions will contribute to the same A-line. The result is an image with a smaller dynamic range. Reducing sidelobe levels is especially important when imaging targets that are less reflective than the surrounding medium such as cysts. There should be very little reflected energy from the cyst depth if the main lobe of a beam is centered over a cyst. There will, however, be reflected energy from the sidelobes. If the sidelobes are large, they will tend to fill in the cyst and make it indistinguishable from the surrounding medium.

Reducing sidelobes in a beam pattern involves using techniques from signal processing. Essentially, synthetic aperture imaging is a sampling application. Instead of using a large antenna or transducer, a small element is translated to cover the aperture of the large antenna. The returns from the small elements are coherently

summed to obtain an approximation of the rf return from the large aperture. In the far-field approximation, the field produced by a given aperture is equal to the Fourier transform of the aperture. Using this fact and the equivalence of convolution and multiplication through the Fourier transform, the effect on the beam pattern of weighting the samples can be seen. An array of elements is formed by convolving a single element with a pulse sequence. Therefore, the field pattern of the array of small elements is the product of the individual element field pattern, which is the Fourier transform of the small aperture, with the Fourier transform of the array, which is a periodic sinc. Further, if the contribution from each element is weighted, then the total field pattern is the convolution of the unweighted pattern and the Fourier transform of the weights.

In array imaging, weighting the individual elements is known as apodization. In signal processing, the same process is called windowing. The theory developed for windowing can be applied to apodization. Signal processing theory shows that the windowing operation will broaden the main lobe and lower the sidelobes of the frequency response. Many common windows are used in signal processing to reduce the ringing effects of truncating the Fourier series representation. Only those used in this thesis will be discussed here. They are the rectangular window, the triangle or Bartlett window, and the Hamming window. A cosine window has also been used for apodization, and it is discussed here. The rectangular window has the most narrow main lobe for a given filter length, but the peak sidelobe level is the highest at -13 dB. The triangle window has a main lobe width twice as wide as the rectangular window, but the peak sidelobe is down -27 dB. The Hamming window has a main lobe width comparable to the triangle window, but the sidelobes are down -43 dB. The cosine window has a slightly more narrow main beam than the triangle window. Its peak sidelobe is higher, but the remaining sidelobes are smaller than for the triangle window. Convolving a signal Fourier transform with one of these windows has the

effect of smoothing the frequency characteristic due to the width of the main lobe. The descriptions of the windows are presented in Table 2.1. The windows and their Fourier transforms are shown in Figures 2.3 and 2.4.

Table 2.1: Window characteristics for length-M windows

Characteristics for Length-M Windows			
Window	Description	Main Lobe Width	Peak Sidelobe (dB)
rectangle	1	$\frac{4\pi}{M}$	-13
triangle	$1 - \left\|\frac{2(n-\frac{M-1}{2})}{M-1}\right\|$	$\frac{8\pi}{M}$	-27
cosine	$\cos(2\pi\frac{n-\frac{M-1}{2}}{\frac{M-1}{2}})$	$\frac{20\pi}{3M}$	-23
Hamming	$0.54 - 0.46\cos\frac{2\pi n}{M-1}$	$\frac{8\pi}{M}$	-43

When using an aperture for transmit and receive, the overall beam pattern is the product of the transmit aperture and the receive aperture. Therefore, the expected peak sidelobe levels of the beam pattern using each of these windows are actually below the main lobe levels by twice the value given in Table 2.1. For example, the expected peak sidelobe level for the rectangular window used in both transmit and receive is -26 dB below the main lobe level.

2.4 Eliminating Grating Lobes

As an application of sampling theory, synthetic aperture beam patterns suffer when the aperture is undersampled. Grating lobes, which are major lobes located away from the desired major lobe, degrade the image quality because reflections from targets illuminated by the grating lobes will contribute to the total reflection for a given position. Grating lobes lower the dynamic range of the imaging system and

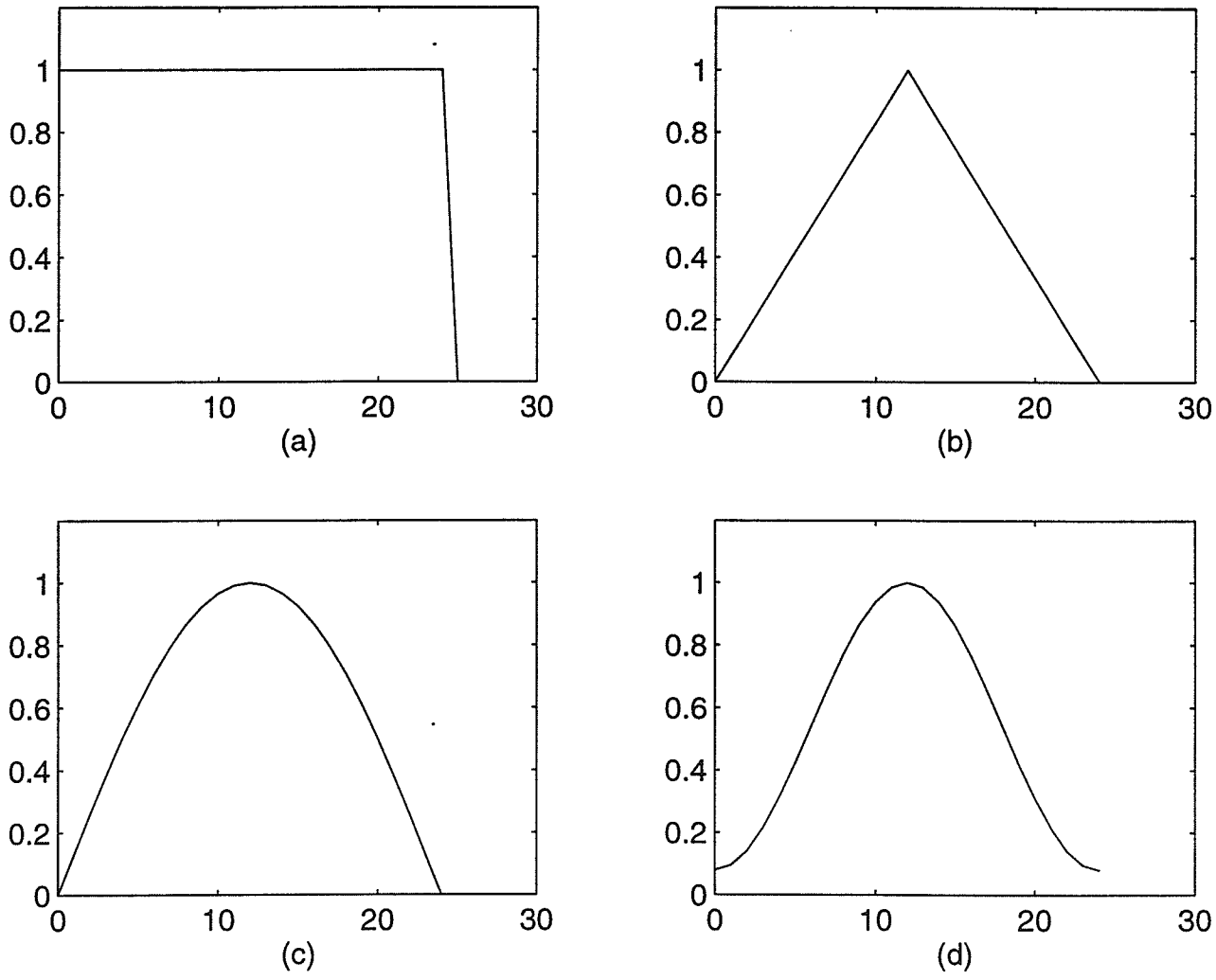

Figure 2.3: Example of apodization weights for windows of length 25, (a) rectangular window, (b) triangle window, (c) cosine window, (d) Hamming window

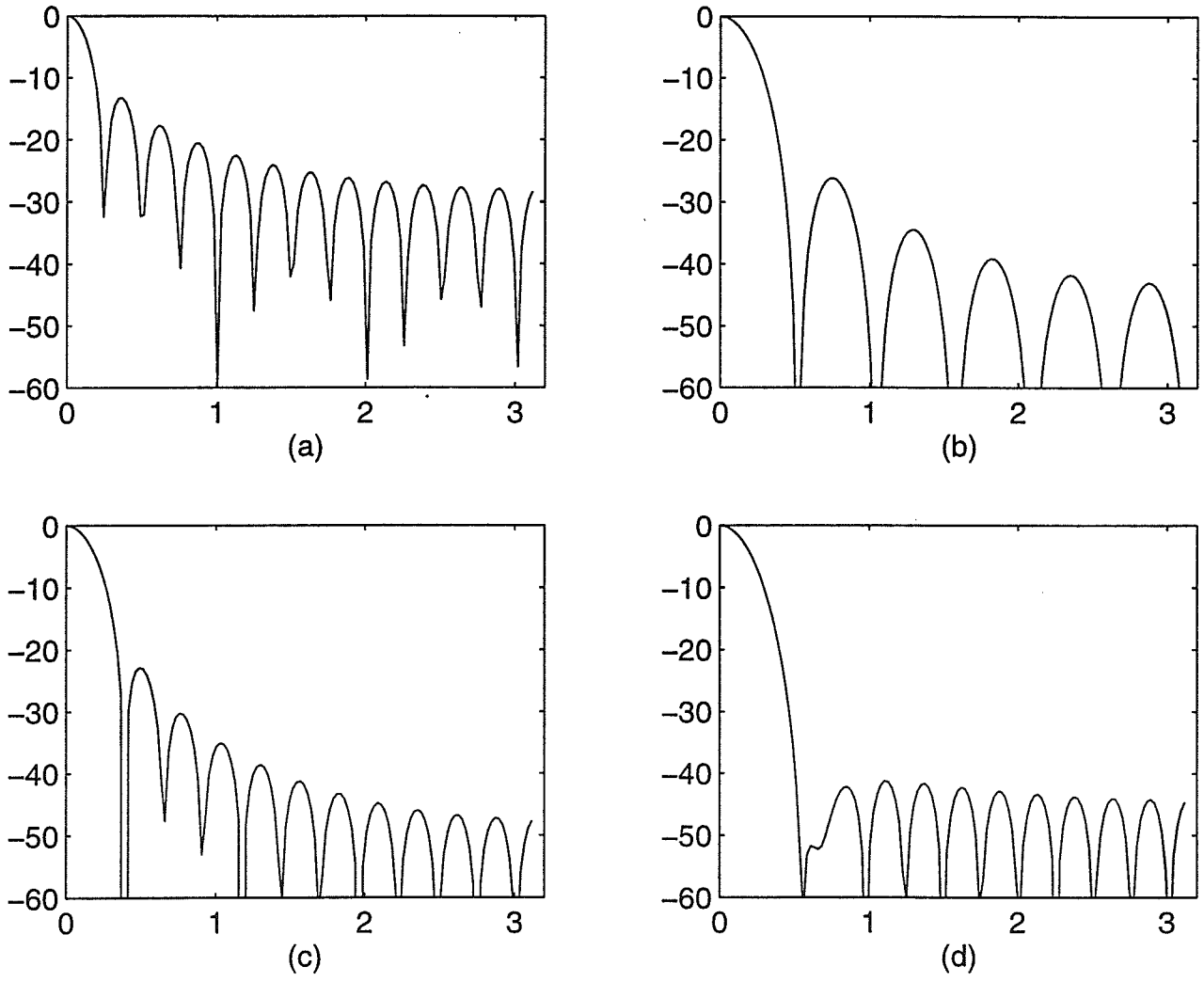

Figure 2.4: Fourier transforms of apodization weights, (a) rectangular window, (b) triangle window, (c) cosine window, (d) Hamming window

contribute to ghost images or copies of a target in the image that also appear at another location in the image. Grating lobes appear in an image when the waves from the individual elements add constructively, not only at the desired location, but also at a location away from the desired focus. To eliminate grating lobes the aperture should be sampled adequately.

Adequate sampling of the aperture depends on the frequency of the transmitted pulse. The imaging situation is depicted in Figure 2.5. To simplify the analysis, the

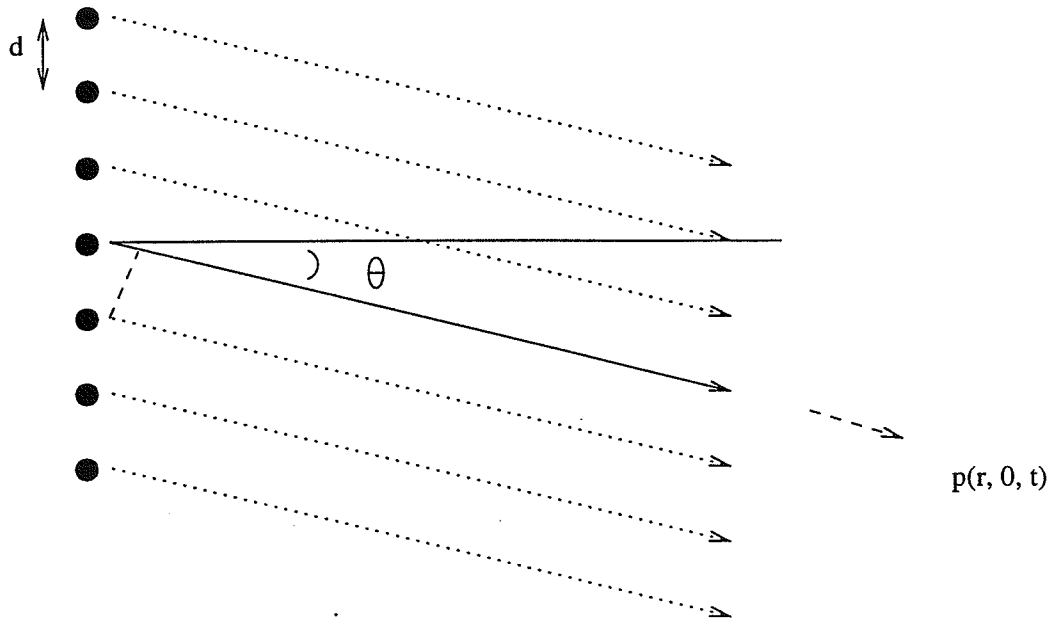

Figure 2.5: Grating lobe formation

individual elements will be assumed to be simple sources. As such, each element has a pattern described by the following equation

$$p_i(r_i, \theta, t) = \frac{A}{r_i} e^{j(\omega t - k r_i)} \tag{2.6}$$

The field pattern for the array is the sum of the individual elements. In synthetic aperture imaging, each element is used for both transmit and receive; therefore, r_i

will be replaced with $2r_i$ to account for the round trip distance. Ylitalo and Ermert refer to this compensation for the round trip distance as replacing λ by $\frac{\lambda}{2}$ [11].

$$p(r,\theta,t) = \sum_i \frac{A}{2r_i} e^{j(\omega t - 2kr_i)} \tag{2.7}$$

If the point of observation is far enough away, the beams from the individual elements can be considered parallel. In the denominator, r_i can be approximated as simply r. In the exponent, that approximation cannot be made since a small error in the magnitude of r_i can create a large difference in phase. Looking at a point at angle θ from the array as shown in Figure 2.5 on page 19, r_i is equal to $r - id\sin(\theta)$. Then the summation reduces to

$$p(r,\theta,t) \simeq \frac{A}{2r} e^{j(\omega t - 2kr)} \sum_i e^{-j2ikd\sin(\theta)} \tag{2.8}$$

Evaluating the sum gives

$$p(r,\theta,t) = \frac{A}{2r} e^{j(\omega t - 2kr - kd\sin\theta(N-1))} \frac{\sin(Nkd\sin(\theta)}{\sin(kd\sin(\theta)} \tag{2.9}$$

The array factor $H_A(\theta) = \frac{1}{N}\frac{\sin(Nkd\sin\theta)}{\sin(kd\sin\theta)}$ is important for determining where grating lobes will occur. Both the numerator and denominator go to zero when $kd\sin(\theta)$ is an integer multiple of π. At these locations, maxima in the beam pattern occur.

$$kd\sin(\theta) = m\pi \tag{2.10}$$

$$\sin(\theta) = \frac{\lambda}{2\pi}\frac{1}{d} m\pi \tag{2.11}$$

$$\sin(\theta) = \frac{m\lambda}{2d} \text{ for m} = 0,\ 1\ \cdots \left\lfloor \frac{\lambda}{2d} \right\rfloor \tag{2.12}$$

To eliminate grating lobes, the interelement spacing d should be made slightly smaller than half a wavelength. No effects of steering the array are considered in this discussion because steering is not used in any processing in this thesis. It can be shown

that if the beam is to be steered -90 to +90 degrees, the distance between elements should not be less than a quarter of a wavelength.

To simplify the analysis, several assumptions have been made in the derivation of the conditions for grating lobes to occur. Using a slightly more complicated approach, the amplitude of the grating lobes will be seen to be reduced. First and most importantly, the sources were assumed to be point sources. For real sources, which have some dimension, the output of the transducer elements is limited in direction. Not all the elements will be able to contribute to the beam pattern at all angles. The actual array response is the product of $H_A(\theta)$ derived above and a modulating factor from the angular response of an individual element. This fact is a result of the Fourier transform property of the far-field pattern. For a circular piston source, the far-field angular pattern is

$$H(\theta) = \frac{2J_1(ka\sin\theta)}{ka\sin\theta} \tag{2.13}$$

where J_1 is the Bessel function of the first kind, θ is the angle between the array and the ray to the point of observation, k is the wavenumber, and a is the radius of the source. This modulating factor will reduce the amplitude of grating lobes at all angles except $\theta = 0$, which is the main lobe.

Second, the transmitted signal is assumed to be a continuous wave. However, for imaging, the transmitted signal is never a continuous wave. In order to obtain a good axial resolution, the transmitted signal should have short duration. Grating lobes occur where the path distance from neighboring elements differs by an integer number of wavelengths. Suppose the transmitted signal is a gated sinusoid of four cycles. The pulses from all the elements will sum in phase at the location of the main lobe because the path lengths are all equal. However, at grating lobe locations, the pulses from at most four elements can add in phase. The pulse from the fifth element will not overlap with the pulse from the first element because they have been

separated in time. This reduces the amplitude of the grating lobe by a factor of $20 \log \frac{N}{4}$ where N is the number of signals that contribute to the main lobe. Only four signals contribute to the grating lobe. The amplitude of the grating lobes can be reduced further by using fewer cycles in the transmitted signal.

Finally, if the transmitted pulse is a burst rather than a gated sinusoid, the grating lobes are further reduced in amplitude because the transmitted pulse is not coherent. The lengths of the pulse that overlap will not match exactly. The combination of all these effects may reduce grating lobes to a level comparable to sidelobes or lower.

2.5 Temporal Undersampling

Image quality is degraded when the data are not adequately sampled in time. Even when the rf data are sampled at the Nyquist rate, the quantized values of the time delays may be too coarse to achieve accurate beamforming. Grating lobes similar to the grating lobes caused by spatial undersampling can appear when the beam focus is steered away from the $\theta = 0$ direction [13]. Even when the beam is not steered, coarse time delays cause an increase in the lateral resolution and an increase in the sidelobe levels.

The general recommendation is that to use the simple delay and sum procedure for beamforming, the signal should be sampled at eight to ten times the center frequency of the transducer, which is much higher than the Nyquist frequency [14]. A good example of how the signal can be degraded is shown in [15]. In the example, four waveforms, each delayed with respect to its nearest neighbor by $\frac{\lambda}{8}$, are sampled at four times their carrier frequency. Then the sampled waveforms are delayed appropriately and summed. This coherent sum is compared to a sum that was created by using analog delays on the original four signals and then sampling the summed signal. The analog delays are considered exact. The first waveform has more than 1 dB less energy

at its carrier frequency than the second waveform. This represents energy that has moved to the sidelobes of the beam pattern.

2.6 Tests to Be Performed

The purpose of this study is to examine whether a virtual source can be used as an actual element to focus an image. In the next chapter, images created with the virtual source are discussed. Further, it is of interest to learn if the behavior of the virtual source is similar to that of an actual source with respect to sidelobes and grating lobes. Once the data have been used to create an image via a simple processing method, the data or the processing are changed to observe the effects.

A set of rf data is collected for tungsten wires in a water tank. Because the wires are smaller than a wavelength, these data can be used to analyze the achievable resolution of the system. Also, these data have no background signal because the water does not reflect the ultrasound. Therefore, these data are useful for measuring sidelobes and grating lobes. Beamwidths and sidelobe levels are measured from these data for each of the different types of windows. Attempts are made to create grating lobes through decimating the data before processing.

Another set of data is collected for nylon wires in a tissue mimicking phantom. These data are useful for observing the system performance when a background signal does exist. In particular, it is used for comparing beam widths of images produced with different windows.

A third set of data consists of returned signals from cyst targets embedded in a tissue mimicking phantom. Here the advantages of different windows are examined for targets that might be filled in by large sidelobes.

CHAPTER 3

EXPERIMENTAL RESULTS

In order to determine the behavior of the virtual source, several synthetic aperture data sets are collected and processed. Various tests are performed to observe the effects of apodization weights, spatial sampling rate, and temporal sampling rate on the quality of the image produced. The results are discussed here; however, before they are presented, the data acquisition system is described, the transducer beam is characterized and compared to the model, conventional B-mode imaging is discussed as a standard for comparison, and the synthetic aperture data sets are described. Following that preliminary work, the virtual source results are presented.

3.1 Data Acquisition

This section presents the system used to collect the data, describes the data sets collected for the synthetic aperture analysis, and shows the results of the transducer beam characterization used for all of the analysis.

3.1.1 Data collection system

The data acquisition system consists of a host PC (ZEOS 66 MHz 486) which is used to control a precision positioning system and retrieve waves from an oscilloscope. A schematic is shown in Figure 3.1. The positioning system is a five-axis system manufactured by Daedal, Inc. (Harrison City, PA), including three translational and two rotational axes. Generally, after the transducer has been manually positioned, only one or two translational axes are used for the scan. Motor controllers for each axis

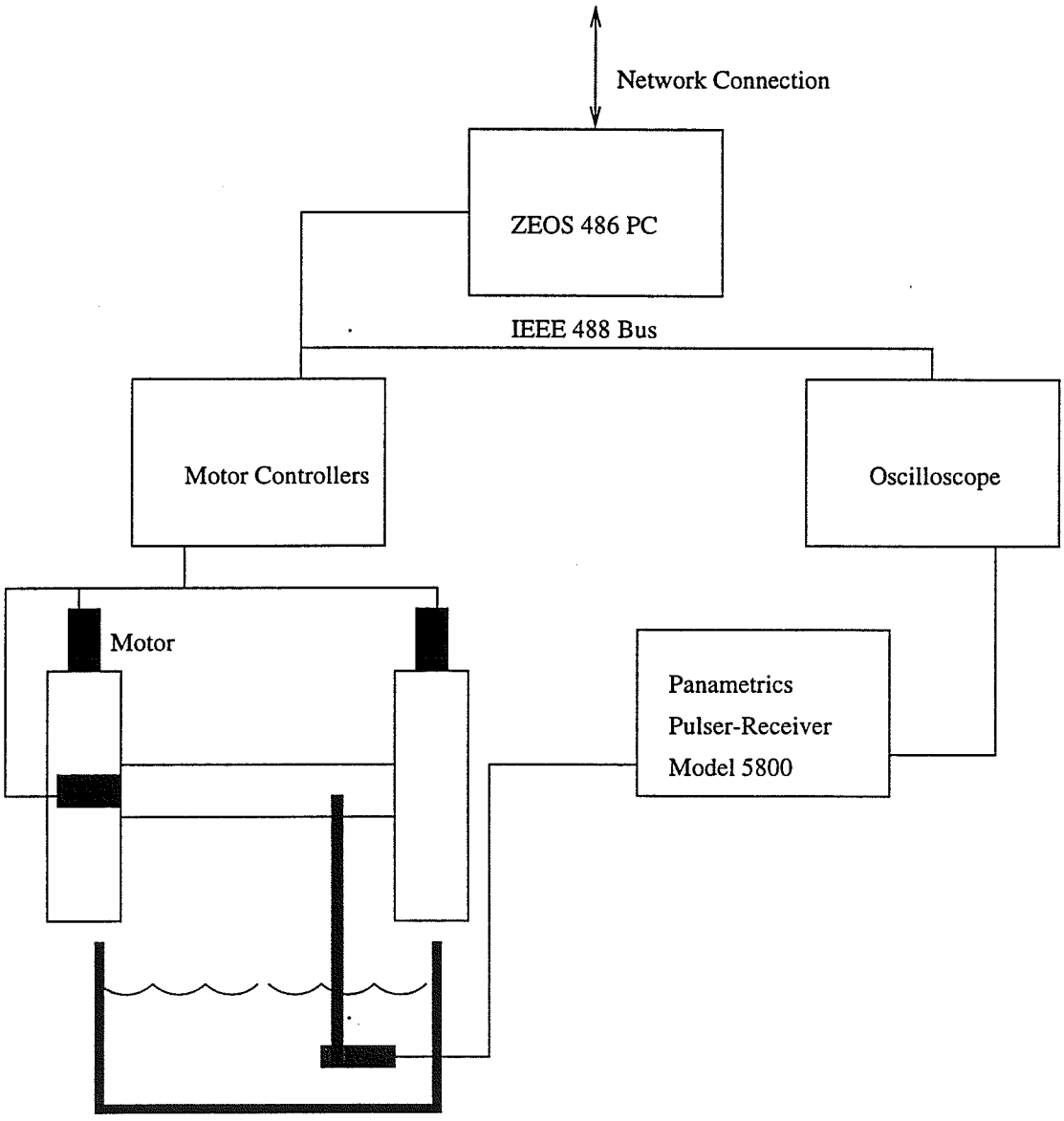

Figure 3.1: Schematic of data collection system

receive commands from the PC via IEEE-488 communications. A Panametrics model 5800 pulser-receiver in pulse/echo mode is used to generate the shock pulses which excite the transducer. The reflected acoustic signal is received by the transducer, filtered by the pulser-receiver and amplified by a gain of 40 dB, and then displayed on either a Tektronix 11401 or a LeCroy 9374L digitizing oscilloscope. The PC retrieves the waveforms from the oscilloscope via IEEE-488 communications and stores them. Then the waveforms are transferred via ftp to a SUN Sparc 20 for processing.

The transducer used in the experiments is a Panametrics 15 MHz focused water-path transducer. It has a 0.5 inch diameter circular aperture and a reported 0.75 inch focal distance giving it an f-number of 1.5. Ideally, the focal diameter would be 150 μm and the focus would be located 19.05 mm from the transducer face.

One data set is collected in a tank of degassed water using a tungsten wire as the target. The wire's diameter is 25 μm, and it is held tautly in position by stretching it across the diameter of a plastic ring. The plastic ring has a diameter large enough that it does not interfere with the acoustic field. This imaging configuration is shown in Figure 3.2.

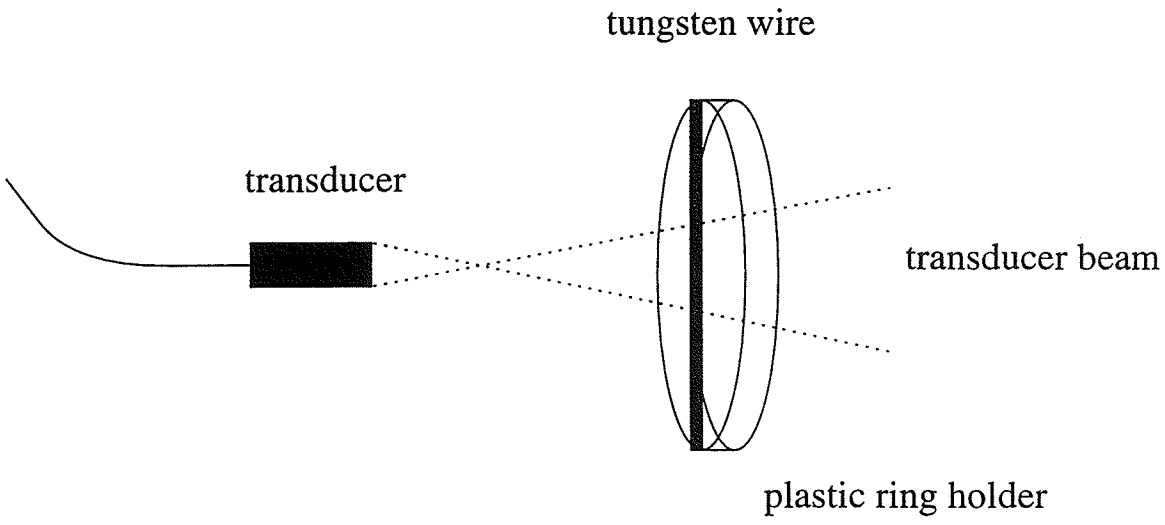

Figure 3.2: Plastic ring holding tungsten wire target

Two other sets of data are acquired using a tissue mimicking phantom as the target. The phantom (ATS Laboratories, Inc., Bridgeport, CT) is made of urethane rubber with a speed of sound of 1450 m/s at room temperature and an attenuation of 0.5 dB/cm/MHz. The phantom contains embedded wire targets and anechoic regions to simulate different imaging scenarios. The wire targets are made of monofilament nylon with a 0.12 mm diameter. The deepest wire in the created images is positioned 1 cm below the phantom surface. The other three wires are each 1 mm closer to the surface and 5 mm to the side of the neighboring wire. A diagram of the wire positions is shown in Figure 3.3. The cyst targets are anechoic regions 2 and 3 mm in diameter, both 1 cm beneath the surface of the phantom. A diagram of these cyst targets is shown in Figure 3.4.

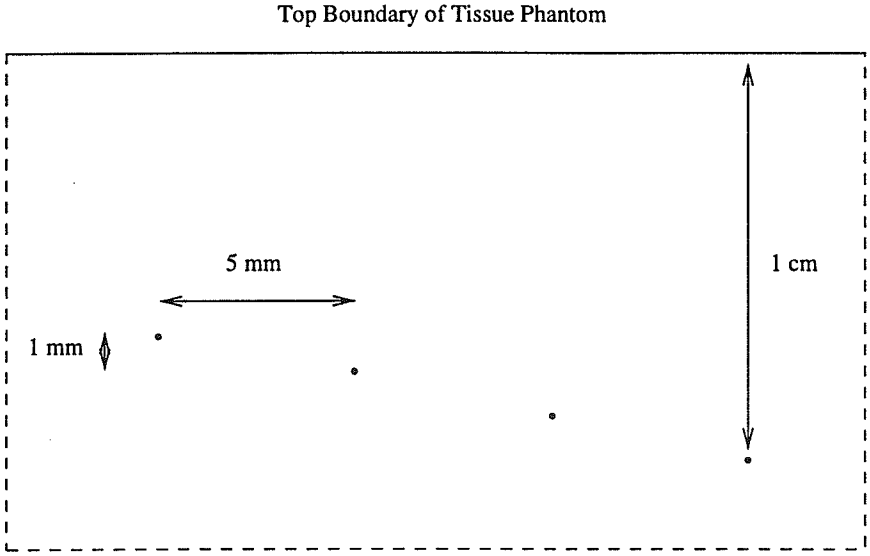

Figure 3.3: Location of wire targets in the tissue phantom

3.1.2 Transducer beam

To accomplish beamforming, the shape of the transducer beam must be known. An experiment is performed to characterize the beam of the transducer used in the

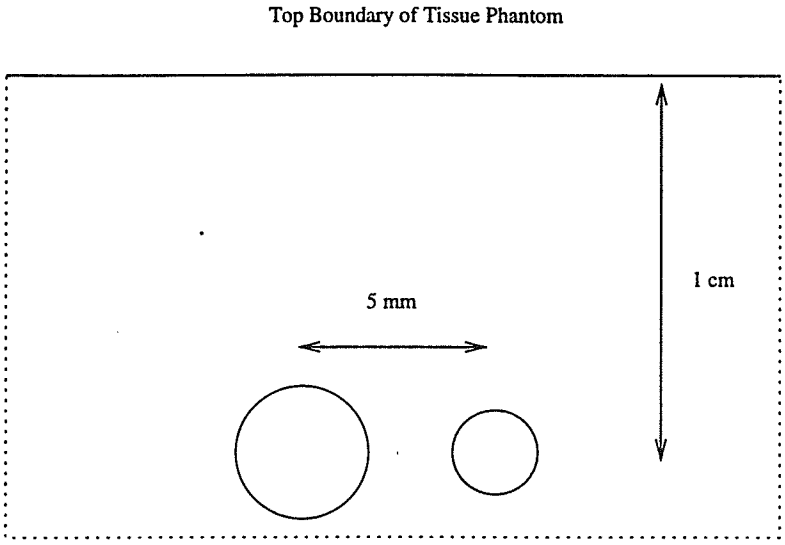

Figure 3.4: Location of cyst targets in the tissue phantom

data collection. The approximate location of the beam's focus is known from data given by the manufacturer. The beam is characterized from a position approximately 0.5 cm in front of the focus to approximately 1.5 cm after the focus using a technique developed in the Bioacoustics Research Laboratory at the University of Illinois at Urbana-Champaign.

The experimental setup is the same as that shown in Figure 3.2 on page 26. Figure 3.5 shows the steps for data collection. The transducer's beam is scanned laterally across a 25 μm tungsten wire, which is held in place by stretching across the diameter of a plastic ring. The maximum value of the signal reflected from the wire is recorded at positions separated by 25 μm for a total of 7 mm. Then the transducer is moved axially away from the wire in 100 μm steps and the lateral scan is repeated. Two hundred axial positions are used. The peak voltage values recorded are stored in a matrix. The beam pattern is shown in a brightness plot with a 50 dB dynamic range in Figure 3.6. It is shown again as a contour plot in Figure 3.7.

Using a Matlab program to find the minimum beam width, it is determined that the focus of the beam occurs at 19.75 mm from the transducer face. This is 0.7 mm

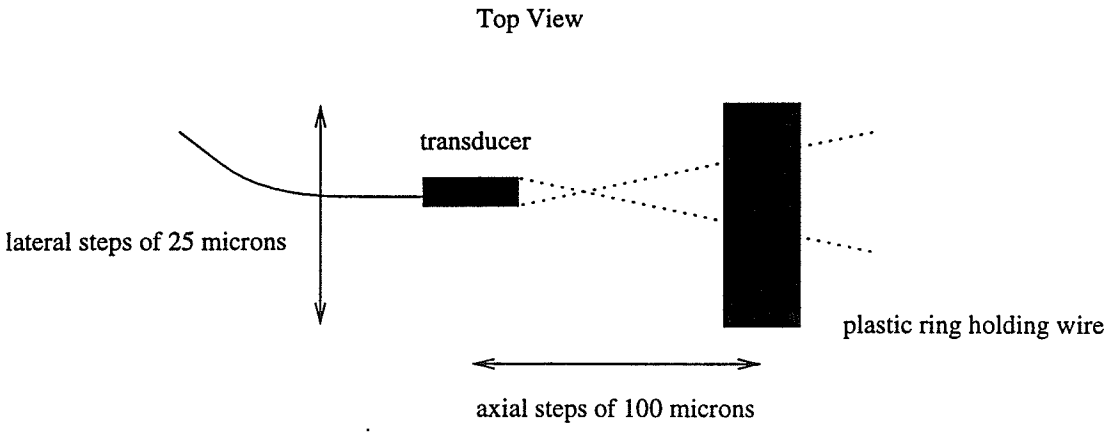

Figure 3.5: Transducer steps to create beam plot

farther away from the source than specified by the manufacturer. The beam width at the focus is 320 μm. The beam is found to initially spread with a half angle of 9 degrees measured at -6 dB and 13 degrees measured at -30 dB points. After 26 mm, the beam does not spread as fast, the half angle decreasing to less than 7 degrees between -6 dB points. These results indicate that the beam spread farther away from the focus is even more limited than what is supposed in the model, although the initial spread is close to what is modeled. From the model, the beam spread is 9.74 degrees between -6 dB points and 19.5 degrees between nulls.

3.1.3 Conventional B-mode data sets

The best image is produced with data collected very close to the focus of the transducer. As a standard for comparison for other data sets, a set of conventional B-mode images are created and analyzed. Using tungsten wires in water as the targets, three images are created; data were taken with the wire located approximately at the focus and at 250 μm and 500 μm farther away from the transducer. Even over this range, a small difference is noticed in the wire beam widths as they appeared in the image. There is also a decrease in the SNR away from the focus. The results are presented in Table 3.1.

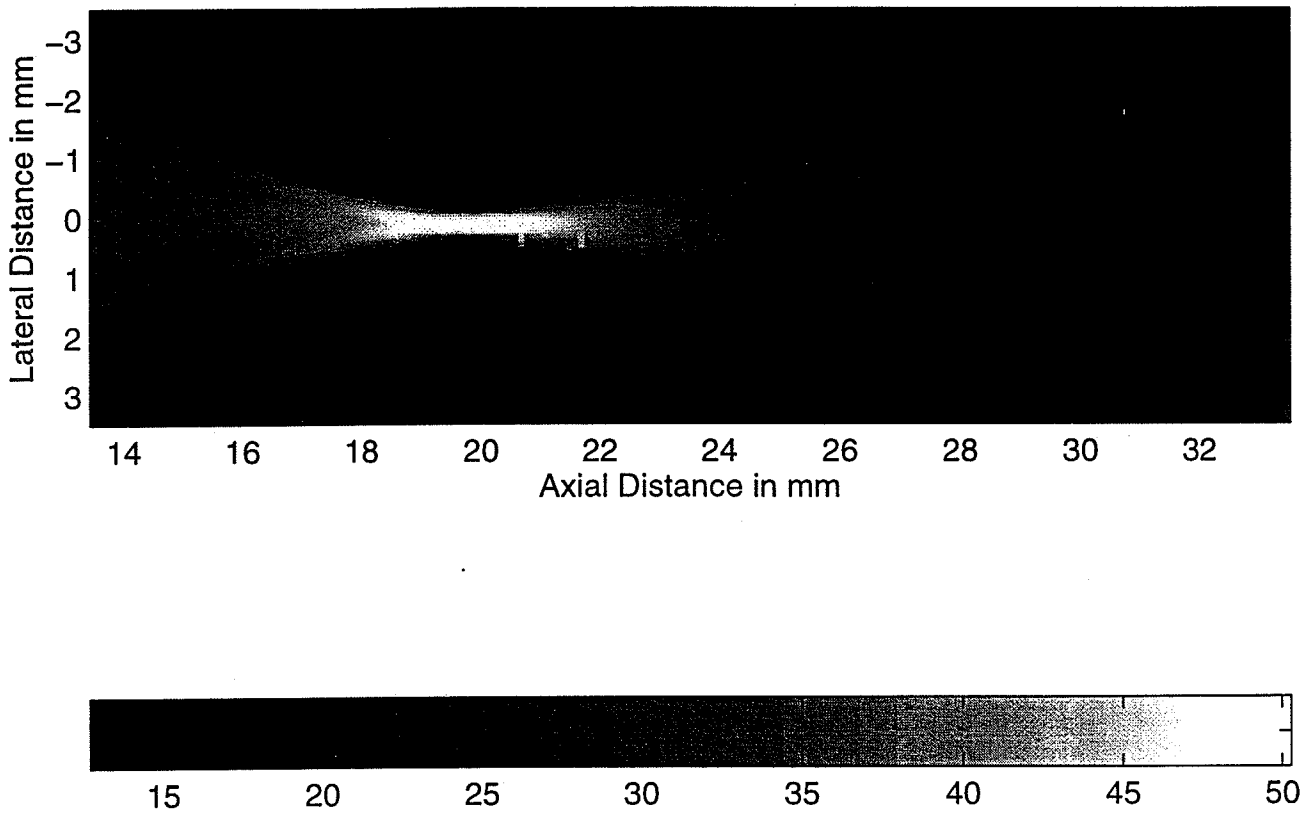

Figure 3.6: Brightness beam plot for the 15 MHz transducer

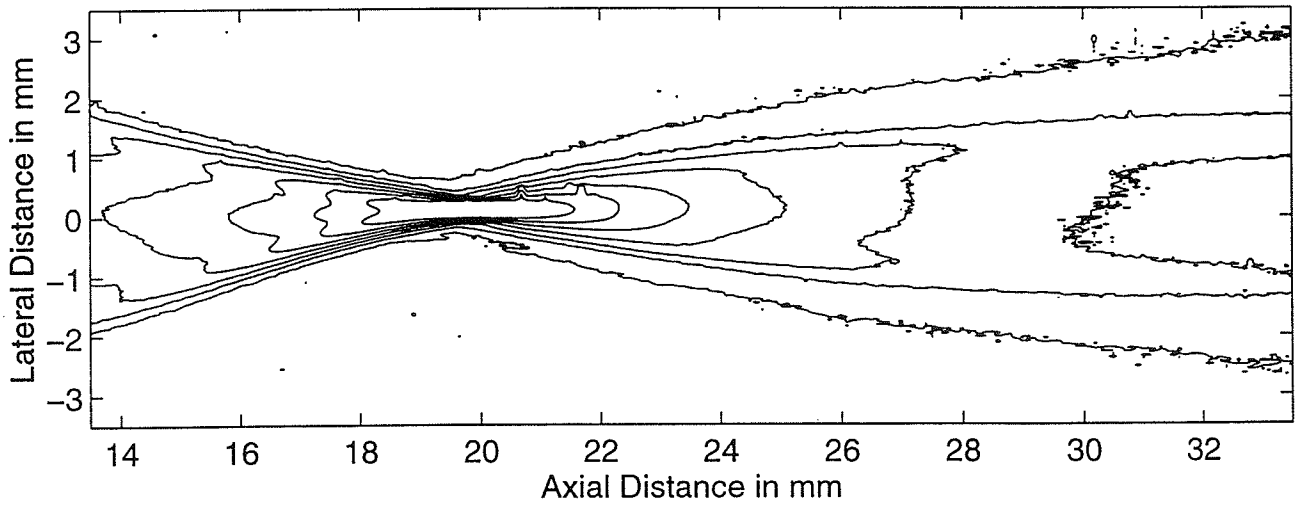

Figure 3.7: Contour beam plot for the 15 MHz transducer

Table 3.1: Measurements on B-mode images

Tungsten Wires Located Near Transducer's Focus			
Wire depth (mm)	20	20.25	20.5
Beam width at maximum (μm)	262	280	292
SNR (dB)	33.3	33.5	35.8

The data for a focused image are also collected using the wires in the tissue phantom. This image is shown in Figure 3.8. The beam widths are measured to be 448 μm, 509 μm, and 549 μm, for the most shallow to the deepest wire.

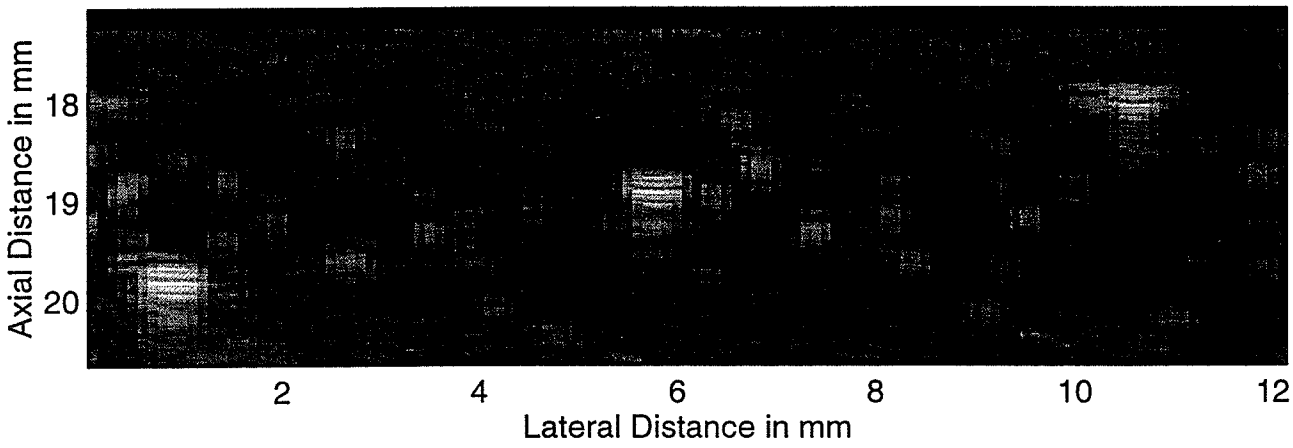

Figure 3.8: B-mode image of wires in tissue phantom near transducer focus

The raw data sets used for synthetic aperture processing illustrate what a conventional B-mode image would produce for targets far away from the focus. Therefore, the raw tissue phantom data are shown here in Figure 3.9. These images have very poor lateral resolution because of the large beam widths at distances far from the focus. At a depth of 1.7 mm from the focus, the beam width is 500 μm; at 3.5 mm

from the focus, the beam width is 1283 μm; and at 5.3 mm from the focus, the beam width is 2030 μm. Obviously an image with near and far targets could be greatly improved by applying some processing to focus the areas away from the transducer focus.

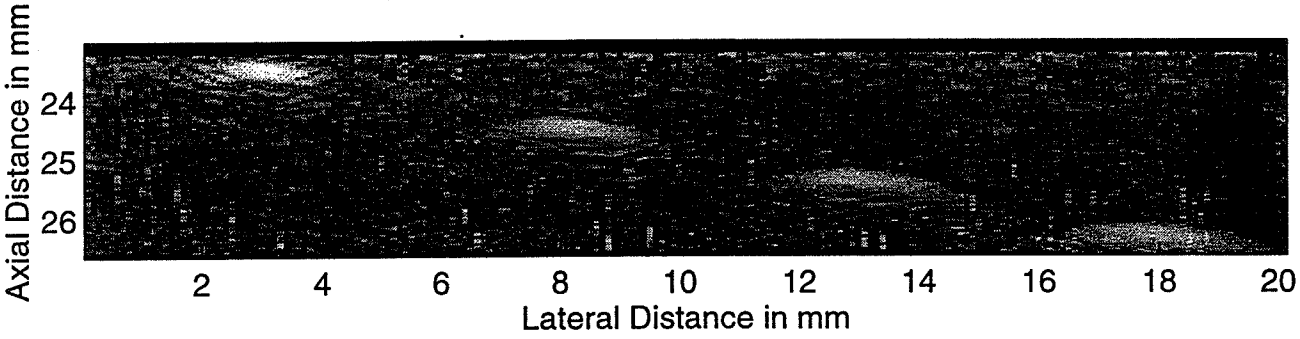

Figure 3.9: B-mode image of tissue phantom data beyond transducer focus

3.1.4 Synthetic aperture data sets

Tests of the image creation from synthetic aperture data are performed on three types of data. First, data are collected using tungsten wire targets in a water bath. The water does not reflect or scatter the sound beam, so this data set can be used for measuring sidelobe levels, grating lobes, SNR, and beam widths. Second, a set of data is collected using a tissue mimicking phantom with embedded wire targets. The tissue phantom contains scatterers which contribute to the background signal; therefore, this data set is used to measure beam widths and signal to background level ratio. Third, a set of data is collected from the tissue mimicking phantom over two cyst targets.

To collect the data set in the water bath, a tungsten wire is held in place by a plastic ring. The transducer is placed a certain distance from the wire so that the wire is at least 1 mm from the focus of the transducer. A single lateral scan is created by positioning the transducer 2.5 mm to one side of the wire and then

moving the transducer in lateral steps of 20 μm recording an A-line at each position. The wavelength is 100 μm, so lateral steps of 20 μm easily satisfy the criterion that samples be spaced less than half a wavelength apart to avoid grating lobes. The transducer is moved axially so that the wire is an additional 2 mm beyond the focus, and the procedure is repeated using a 6 mm lateral scan distance. A third lateral scan is performed with the transducer located an additional 3 mm from the wire. The lateral scan distance for this third scan is 7 mm. The rf data are digitized at 256 MHz using a Tektronix 11401 digitizing oscilloscope. This sampling rate is more than ten times the center frequency of the transducer, which will lead to finely quantized and accurate delays.

The second set of data is collected in the following way. The transducer is placed at a distance above the phantom so that the signal of interest, the reflection from the wires, is not hidden in the reflection from the surface of the phantom. The focus of the transducer is beneath the surface of the phantom. This configuration is shown in Figure 3.10. The transducer is scanned laterally from the wire closest to the surface to the wire farthest from the surface. A-lines are collected with a spacing of 100 μm, equal to one wavelength in water for the 15 MHz transducer. The rf data are digitized at 250 MHz using a Lecroy 9374L digitizing oscilloscope.

The cyst data are collected in a similar manner. Again the focus of the transducer is located beneath the surface of the phantom. A-lines are collected 50 μm apart for a total lateral scan distance of 2.5 cm. They are digitized at a rate of 204.8 MHz using the Tektronix 11401 digitizing oscilloscope.

3.2 Data Processed with Uniform Weights

The delay and sum processing with uniform apodization weights is evaluated first on the tungsten wire data. A C program is used to perform the delay and sum beamforming. The beam width, sidelobe level, and SNR at each depth are presented

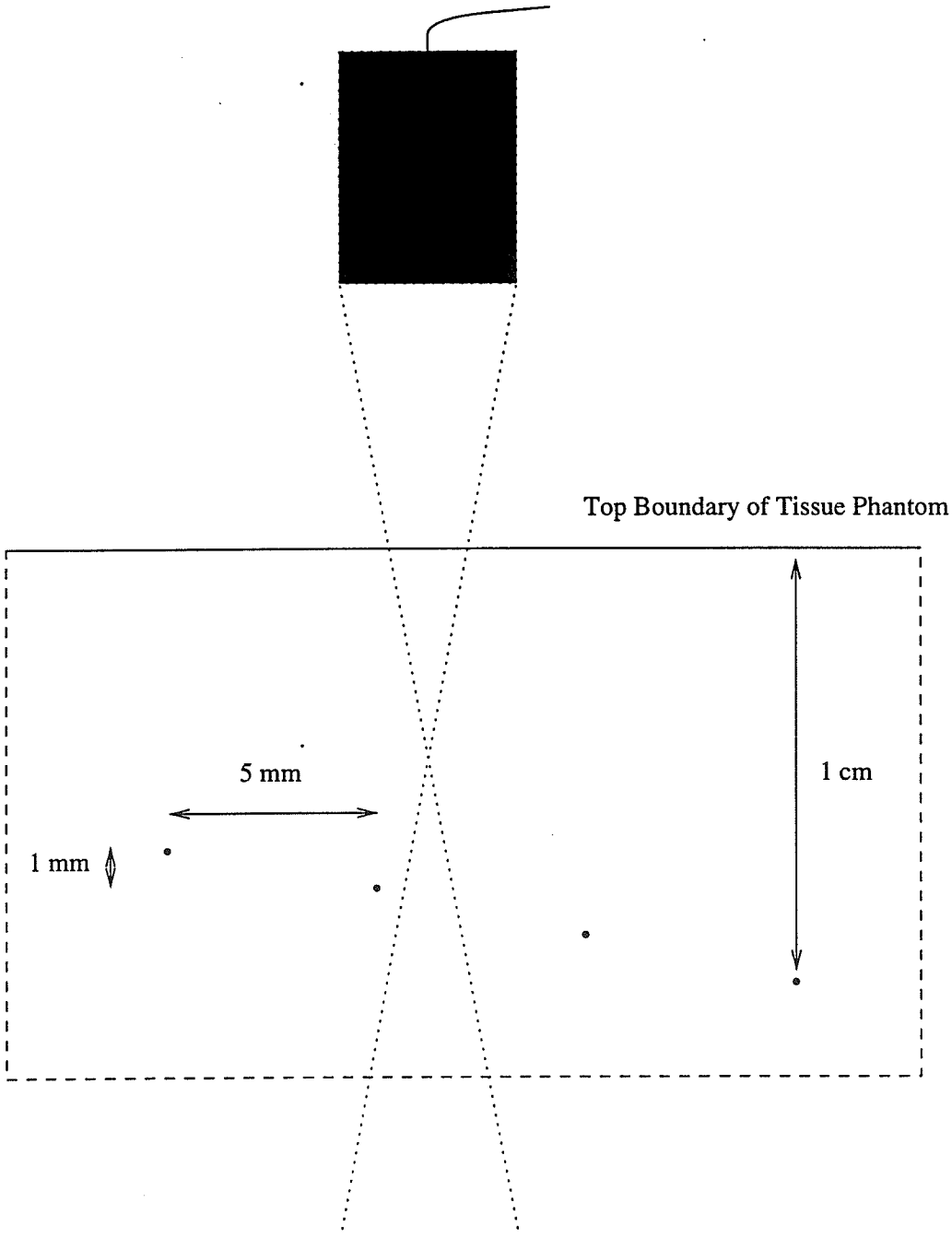

Figure 3.10: Position of focus for imaging tissue phantom targets

in Table 3.2. A sample of a beam profile is shown in Figure 3.11. The minimum beam widths indicate that the system achieved an f-number between 2 and 3. The beam widths, measured at the depth of maximum brightness, which range from 275 to 340 μm, are a good match with the average beam width of 278 μm measured from the conventional B-mode image.

Table 3.2: Tungsten wire data processed with uniform weights

Tungsten Wire Image Characteristics			
Wire depth (mm)	1.7	3.5	5.3
Minimum beam width (μm)	227	209	234
Beam width at maximum (μm)	275	304	340
Sidelobe level (dB)	-22.1	-28.3	-28.3

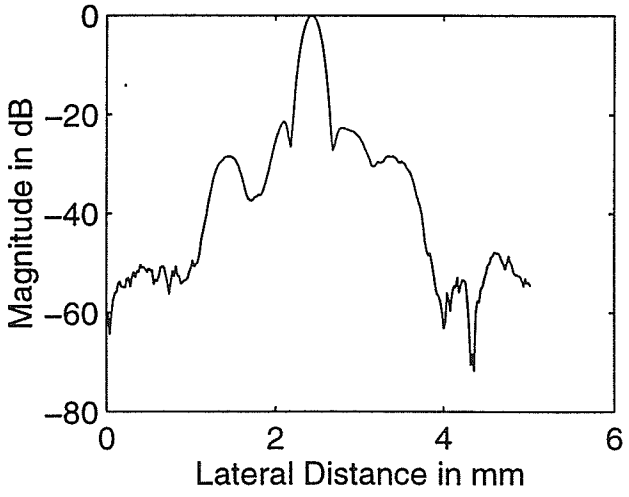

Figure 3.11: Sample beam profile taken from most shallow tungsten wire

An image shown in Figure 3.12 is created from the wire data collected with the tissue mimicking phantom. The beam widths and ratio of signal to background level

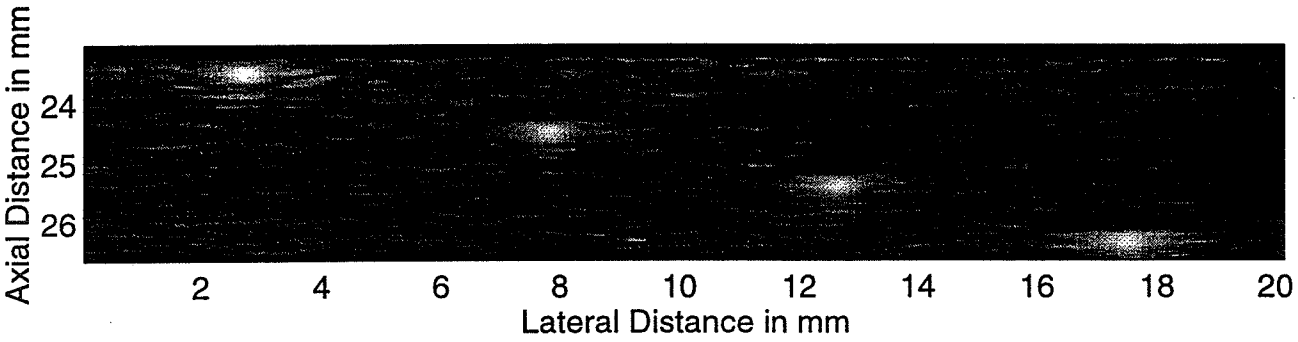

Figure 3.12: Image produced from tissue phantom data with uniform weights

calculated from these data are displayed in Table 3.3. Here the ratio is not the SNR because the background level is not noise. It represents scattered signal from the urethane rubber, which is intended to mimic the scatter from liver tissue. The signal to background level ratio is calculated in the same way as an SNR. Using data that have not been logarithmically compressed, the root mean squared (rms) pixel value is calculated for a small region over each wire target. The rms pixel value is also calculated for four small regions where there is no signal from the wire target and no sidelobes. The values from each region are averaged. The SNR is calculated for each wire in the image by taking

$$SNR = 20 \log \left(\frac{\mu_s}{\mu_{n,ave}} \right) \tag{3.1}$$

where μ_s is the rms pixel value over the wire and $\mu_{n,ave}$ is the average rms pixel value over the four regions of no signal. Then the average SNR for the image is calculated by averaging the values for each of the wire targets in the image. This is the same procedure followed by Karaman et al. in [7]. For the wires in the tissue phantom processed with a rectangular window, the overall SNR is found to be 25.10 dB. The 6 dB beam width, which is considered a good indication of the lateral resolution,

remains nearly constant over the range in the image. The first wire has a beam width of 619 μm. The second, third, and fourth wires have beam widths of 616, 624, and 619 μm, respectively. The wires actually have a width of 120 μm.

Table 3.3: Tissue phantom data anaylzed with uniform apodization weights

Tissue Phantom Image Characteristics				
Wire number	**1**	**2**	**3**	**4**
Minimum beam width (μm)	619	616	624	619
Beam width at maximum (μm)	711	731	820	862
Signal to background ratio (dB)	23.29	23.61	27.08	26.43

3.3 Data Processed with Other Weights

The simple delay and sum approach can be improved by reducing the sidelobes in the beam pattern, thereby improving the SNR. Several common apodization weights are used with various tradeoffs in main lobe width and sidelobe height, affecting both lateral resolution and SNR. In this study, triangle, cosine, and Hamming windows are used. Both sidelobe levels and lateral resolutions are presented for the wires in water data in Table 3.4.

Applying the weights widens the beam width and lowered the sidelobes, which is the expected result. At all three depths considered, the cosine window increases the beam width by the smallest amount, and the Hamming window reduces the sidelobes by the largest amount. The relative beam widths for the wires at different depths are also maintained. In other words, the second wire has the smallest beam width of the three wires after processing with any window. The third wire always has the widest

Table 3.4: Tungsten wire data analyzed with nonuniform weights

Tungsten Wire Data Analyzed with Windows			
	Min Beam Width (μm)	Beam Width at Max (μm)	Sidelobe Level (dB)
triangle			
1	338	394	-40.1
2	313	442	-38.4
3	315	476	-23.8
cosine			
1	325	377	-38.1
2	293	416	-36.3
3	306	447	-29.6
Hamming			
1	361	416	-44.3
2	332	461	-40.1
3	330	487	-26.1

beam width. The sidelobes are reduced with each of the different windows. The most improvement occurs for the shallowest wire, and the least for the deepest wire. The performance of the cosine and triangle windows are comparable.

Figure 3.13 shows the images produced from the tissue phantom data. The modified lateral resolutions for the tissue phantom are listed in Table 3.5. The results are similar to the tungsten wire data results. The wire beam widths increase after processing with the windows. There is not much difference between the results from the triangle and cosine windows. The Hamming window forces a greater increase in the beam width than the other two. In this set of data, the sidelobes are already below the noise floor, so the sidelobe levels are not measured. The signal to background level ratios do not change significantly with the application of the window weights.

Table 3.5: Tissue phantom data analyzed with nonuniform weights

Tissue Phantom Data Analyzed with Windows				
wire number	**1**	**2**	**3**	**4**
Minimum beam width				
triangle	765	837	836	901
cosine	769	841	845	889
Hamming	790	882	909	986
Beam width at max				
triangle	830	896	932	977
cosine	852	891	926	942
Hamming	879	944	975	1013

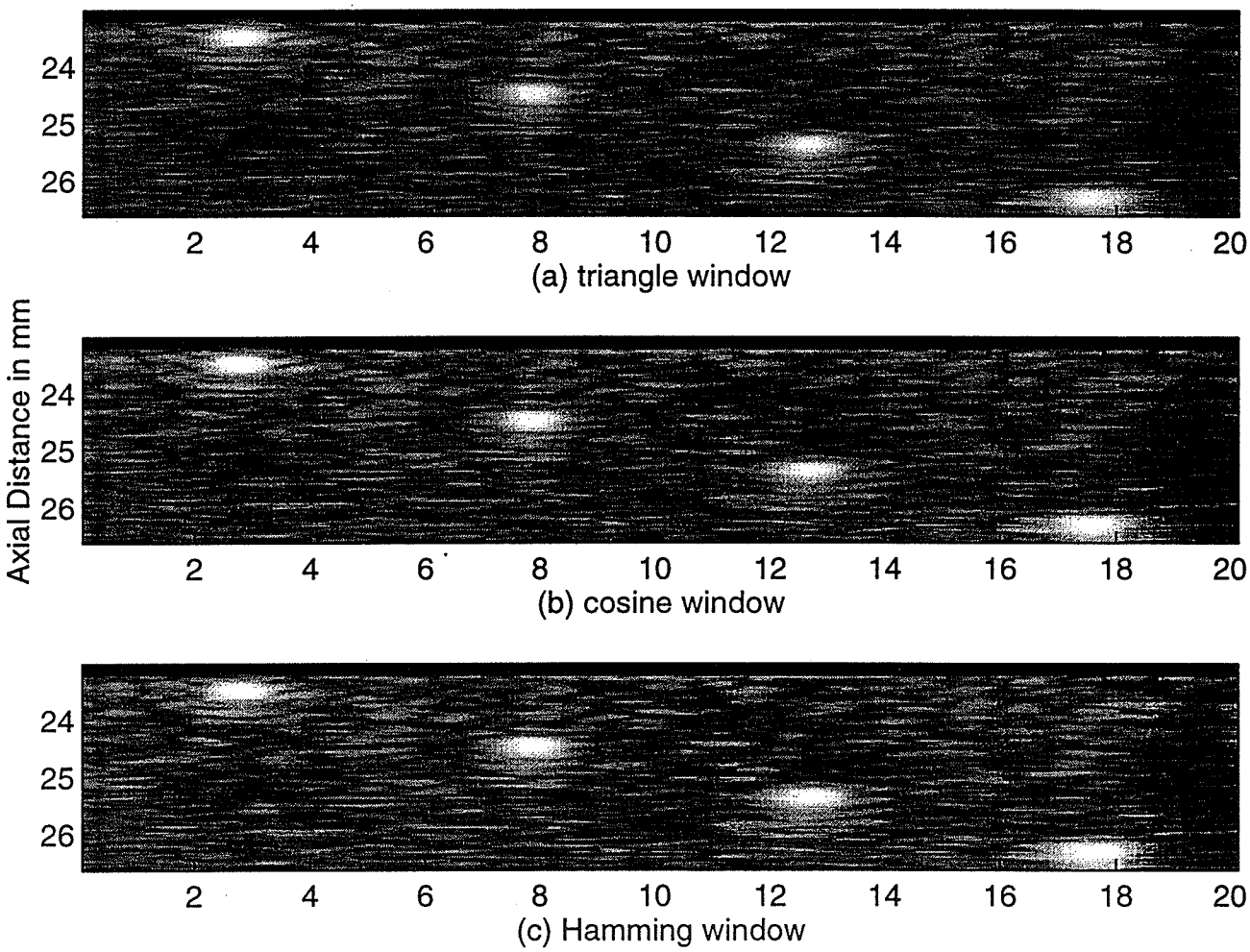

Figure 3.13: Images produced by delay and sum processing with three windows, (a) triangle window, (b) cosine window, (c) Hamming window

3.4 Cyst Data

Even though both voids and wire targets represent large impedance mismatches for the ultrasound signal, wire targets are more easily distinguished in an image. When the main lobe is over the cyst, there are sidelobes over regions that do reflect sound. Therefore, the region inside the cyst does not appear completely dark as it should. The signal reflected by the sidelobes instead appears to have been reflected from inside the cyst. This blurring of the cyst is referred to as cyst fill-in. Obviously, the larger the cyst, the less of a problem this is since more of the field can be incident on the cyst and not the surrounding regions.

Cyst data are used to compare the performance of processing with a rectangular window and processing with other windows. The amount of cyst fill-in gives a qualitative measure of the main lobe beam widths and the sidelobe levels.

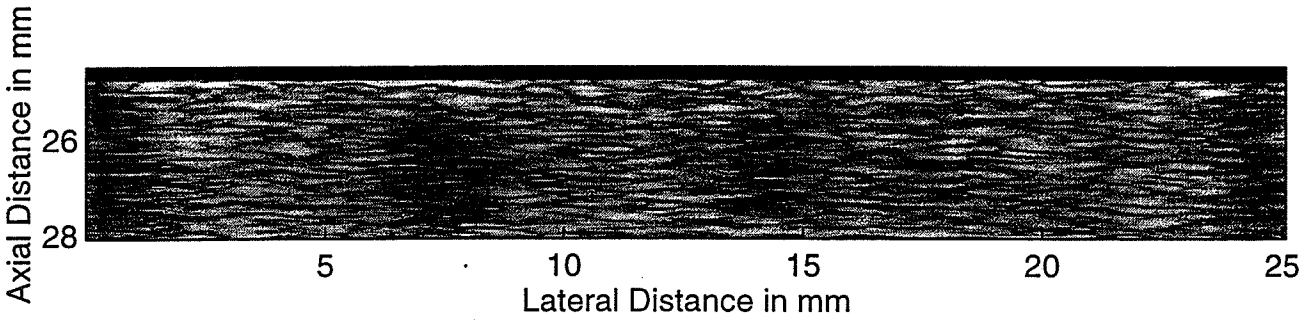

Figure 3.14: Image produced with delay and sum processing and uniform apodization weights from cyst data

The image produced using the rectangular window or uniform weights is shown in Figure 3.14. In order to quantify the quality of this image, a contrast to noise ratio (CNR) is calculated for each target. The formula used is the same as that used by Karaman et al. in [7].

$$CNR = \frac{|\mu_c - \mu_b|}{\sigma_b} \tag{3.2}$$

where μ_c is the mean intensity of the cyst in dB, μ_b is the mean of the background,

and σ_b is the standard deviation of the background. As expected, the CNR is greater for the larger cyst than for the smaller one, because it is easier to isolate a large cyst in the main lobe of a beam than a small one. Quantitative values of CNR are presented in Table 3.6 for the rectangular window and the other windows. The images produced by processing with nonuniform weights performed better than the rectangular window; however, there is not much difference in the performance of the individual windows when compared to each other. Images are shown in Figure 3.15.

Table 3.6: Contrast to noise ratio for cyst targets

Contrast to Noise Ratios		
Window	2 mm cyst	3 mm cyst
rectangular	1.58	1.83
triangle	1.78	2.08
cosine	1.78	2.07
Hamming	1.72	2.01

3.5 Grating Lobes

In order to test the necessity of collecting signals from transducer positions located less than half a wavelength apart, the data are decimated in the lateral direction. Instead of having 351 A-lines for the farthest tungsten wire, images are produced with 176, 117, 71, 51, and 36 A-lines corresponding to decimation by factors of 2, 3, 5, 7, and 10, respectively. This experiment is performed only with the tungsten wire data to avoid confusion of grating lobes with background scattering. No grating lobes are found for data sets decimated by 2, 3, or 5. Grating lobes are not expected for

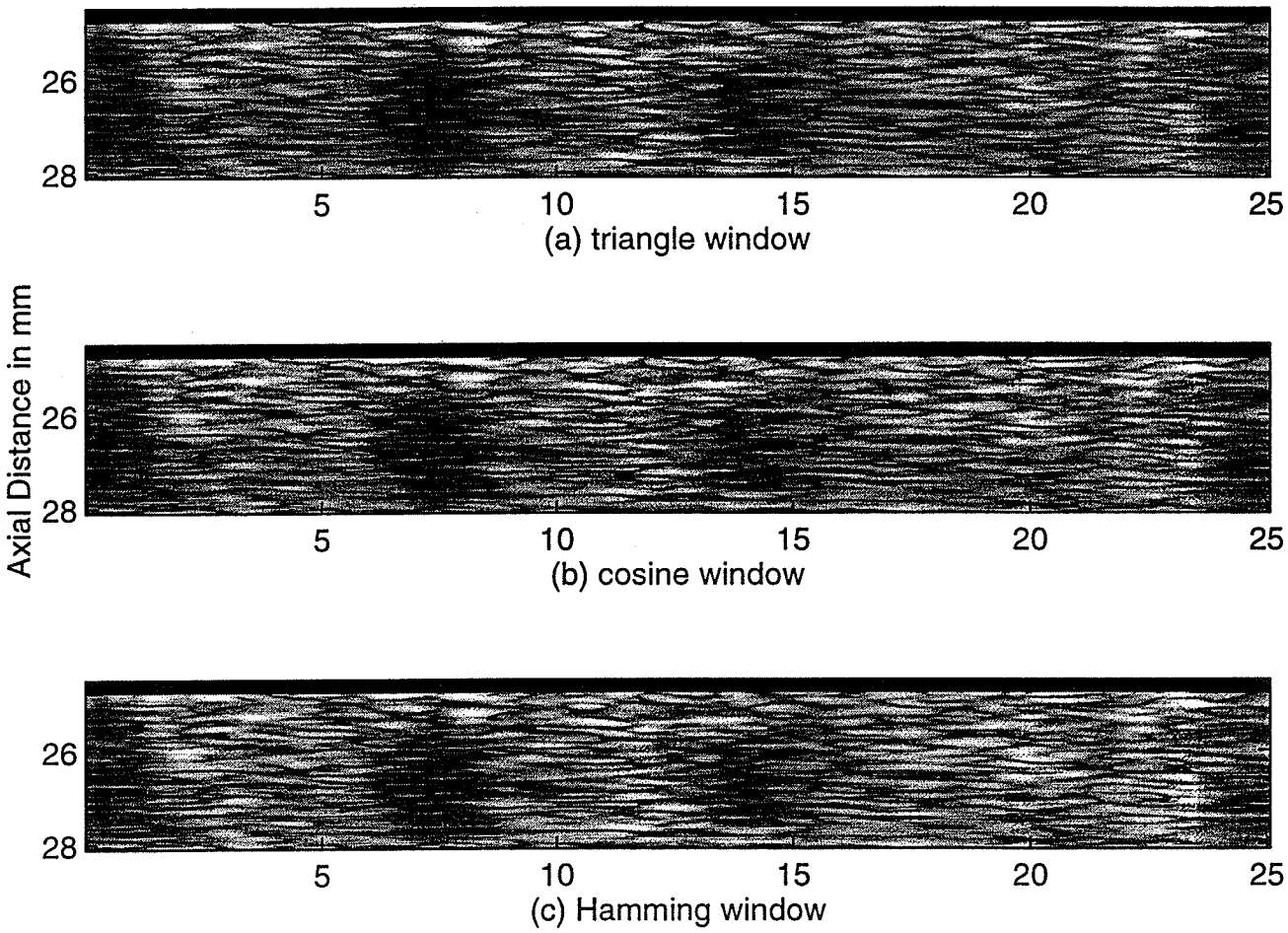

Figure 3.15: Images produced from cyst data with delay and sum processing, and nonuniform weights, (a) triangle window, (b) cosine window, (c) Hamming window

the image decimated by 2 because the spatial sampling at this rate is 40 μm, which is still less than half of a wavelength. Even decimating the data by 3 gives a sampling rate close to the half wavelength limit. By the development in Chapter 2, grating lobes that exist when the data are sampled one wavelength apart would appear at 30 and 90 degrees. Here, no change in the image is expected from the grating lobes at 90 degrees because there is no target at this location to interfere in the image. However, it would be possible to see a response from a grating lobe that appears at 30 degrees. Because the focus has a finite width, the grating lobe at 30 degrees is expected to be down by 18.6 dB. There is an additional reduction in the size of grating lobes because the image is created with a pulse rather than a continuous wave. The minimum number of elements used to create a block of the image is 17. The pulse has a length of approximately three wavelengths. This corresponds to a reduction of 15.0 dB. Therefore, even though grating lobes may exist, they do not rise above the noise level in this image.

Grating lobes are observed for the images created from the data decimated by factors of 7 and 10. In the image decimated by 7, the measured grating lobe has a magnitude 31.9 dB below that of the main lobe. It is located at 20.9 degrees. There, the reduction due to the directivity of the main beam is 17.7 dB, and the reduction due to the pulsed waveform is 12.7 dB for a total level of -30.4 dB. Further reduction that appears in the image may occur because the pulse is not a single frequency, so even when the pulses from neighboring elements do overlap, they do not overlap exactly. Therefore, the expected gain is not achieved. For the image decimated by a factor of 10, the grating lobes are observed at 14.5 degrees. These grating lobes are shown in Figure 3.16. They have an average magnitude of 24 dB below the main lobe. Here the reduction due to the limited beam is 7.10 dB, and the reduction due to the pulse length is 9.54 dB for a total reduction of 16.64 dB. Again the grating lobes are smeared, because of lack of coherence in the pulse contributing to total

measured reduction. With this decimation factor, the grating lobes cover a large area and, therefore, do not reach as high a level as they could theoretically.

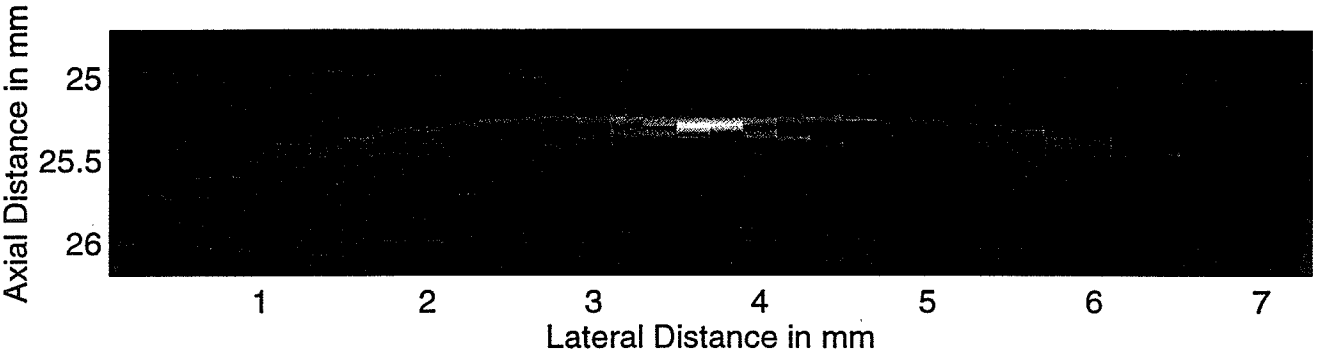

Figure 3.16: Grating lobes that appear when A-lines are collected two wavelengths apart

These results follow from the observations made in the second chapter in which it is shown that grating lobe magnitudes decrease as a result of using a directional element and using a pulsed signal instead of a continuous wave. The beam spread of the virtual source is not very large; therefore, it can be considered a directional source.

3.6 Temporal Sampling

Undersampling the data temporally degrades the image quality. Using the tungsten wire data for the wire at 3.5 mm, the data are decimated in the axial direction. The original data are sampled at a rate of 256 MHz, which is greatly oversampled given that the center frequency of the transducer is 15 MHz. Accurate delays can be made because of the high oversampling. However, at sampling rates only slightly greater than the Nyquist sampling frequency, the delays are not accurate enough to result in good beam forming. In order to demonstrate the degradation to the image if the data are not sampled at a high enough rate, the data are decimated by factors of 2, 4, 6, and 8, giving sampling frequencies of 128, 64, 42.67, and 32 MHz. The last

example is not actually above Nyquist because the transducer has a bandwidth of approximately 10 MHz; the highest frequency carrying signal is 20 MHz, and therefore the Nyquist frequency is 40 MHz.

No grating lobes are observed after axially decimating the data because no steering is attempted. However, the image quality has been degraded. For the tungsten wire at 3.5 mm from the virtual source with data sampled at 256 MHz, the beam width at the depth of maximum brightness is 304 μm. The corresponding beam widths with the subsampled data were 307, 309, 331, and 1051 μm, respectively. The last width is much worse than the other three because the sampling rate does not even satisfy the Nyquist criterion. The degradation occurs because accurate delays cannot be made.

3.7 Discussion

Experiments were performed for this study which parallel the experiments used for array elements. The virtual source behaved as a real transducer element would in response to synthetic aperture processing techniques. Beam forming processing was able to focus the beam to a level comparable to that of an actual focused element. The minimum beam widths were produced with uniform apodization weights. Sidelobe levels, however, were reduced using nonuniform weights. Grating lobes were not a problem as long as the spatial sampling rate was at most one A-line per wavelength. The temporal sampling rate was found to be a factor that determined image quality. These conclusions have been reached in studies of ultrasonic imaging with transducer arrays. Therefore, the focus of a mechanically focused transducer may be used as a virtual element to focus the rest of the image. Conventional B-mode images can be improved by applying SAFT to the region beyond the focus.

CHAPTER 4

CONCLUSIONS

4.1 Conclusions

The results presented in Chapter 3 show that it is possible to treat the focus of a transducer as a virtual element for the sake of synthetic aperture processing. Once the beam pattern of the transducer has been determined, SAFT processing can be performed without regard to whether or not the element actually exists. To make the same improvements, the modifications that have been made to delay and sum beamforming with actual elements can be applied to images created with virtual sources. Although the experiments in this thesis are performed with a tissue mimicking phantom, the application of the result is not limited to medical imaging. Other ultrasonic imaging applications, such as nondestructive evaluation and subsurface imaging, can also potentially benefit from this work. The results are further applicable to other imaging systems where synthetic aperture techniques are used such as radar and sonar. The following sections present limitations found in the course of the study and logical extensions of this work.

4.2 Limitations of Beam Spread

As stated several times in this thesis, sources for synthetic aperture imaging should be small, giving rise to a wide beam spread. The more focused a transducer is, the wider the beam spread it will have beyond the focus. In this thesis, the transducer used is considered to be highly focused, with an f-number of 1.5. Still, the lateral

resolution achieved by the imaging system is not ideal. The resolution achieved is approximately three times the wavelength. Generally the desired resolution is less than twice the wavelength. Although the resolution is much better than that of the focused beam outside the depth of focus for a conventional B-mode image, it does not compare to the resolution at the focal point or the resolution reportedly achieved by array transducers. This implies that to achieve good focusing with a virtual source, the transducer should be even more focused, perhaps with an f-number less than one.

4.3 Dimensionality of the Problem

Essentially the problem studied in this thesis is two dimensional. The targets in each experiment are line targets rather than point targets; they only vary in two dimensions, along the range and along the direction of the lateral scan. Because the targets being imaged do not vary in the third dimension, perpendicular to both the lateral scan and axial depth, only one scan is necessary to resolve the scene. If the targets had been point targets which varied in three dimensions, data would have to be collected for a matrix of transducer positions, not just a line in order to resolve the scene.

4.4 Phase Aberration

One of the major assumptions of this thesis is that the speed of sound is constant in the medium that is being imaged. For the tungsten wire data and tissue mimicking phantom data considered here, this is true. However, in medical or subsurface imaging, the speed of sound is not constant. In the body, different tissues have different speeds of sound ranging from 1450 m/s for fat to 1580 m/s for liver. In subsurface imaging, changes in soil compaction and moisture content will affect the local speed of sound. This local variability of the wave speed gives rise to what is known as the phase aberration problem. The delays used to create a focused beam

cannot be calculated simply on geometric concerns. The goal is to have the pulses from all the elements arrive at a point at the same time. The actual delays contain some perturbation due to the variation in the speed of sound. Here that perturbation to the geometric delay is called the aberration delay.

Several researchers in the medical ultrasound community have studied the phase aberration problem as it applies to a layer of tissue with a different speed of sound, such as with a layer of fat in the abdomen. Several methods for phase aberration correction with varying degrees of efficacy and computational complexity have been suggested. In general, methods attempting to adjust for phase aberration involve finding the relative time delay between neighboring elements. In 1988, Flax and O'Donnell [16] proposed using the correlation between returned signals from two adjacent array elements to calculate the aberration delay. The aberration delay equals the time where the signals have the maximum correlation coefficient. This method corrects aberration in one iteration if the signals are reflected from a point target, but the method also works if the target is a diffuse scatterer. In that case, it requires three iterations. In 1989, Trahey [17] proposed a method that uses the area wide target brightness as a measure of how well the phase aberrations have been corrected. Because phase aberration prevents a good focus from being formed, the brightness of a region in a diffuse scatterer is decreased by phase aberration. Fixing the phase will result in higher pixel brightness. Delays are adjusted until a maximum is found. In 1991, Karaman et al. [18] discussed a lower complexity technique to calculate the aberration delay between two adjacent elements. The relative delay between the signals received by two elements is the amount that one signal is delayed with respect to the other that minimized the sum-absolute-difference of these signals. The aberration delay is the difference between that relative delay and the delay calculated for focusing.

Despite the amount of research that has explored the problem of phase aberration,

no good compromise between quality of correction and complexity has been found. Now that virtual sources have been shown to be good sources for beamforming, the phase aberration problem should also be studied using them as sources.

4.5 Transducer Arrays

Much of the work in ultrasonic medical imaging and subsurface imaging uses transducer arrays to collect the data. With transducer arrays, the signal to noise ratio can be improved by firing more than one element at once to increase the output power as shown by Karaman et al. in [7]. Grating lobes can be lowered with a less restrictive condition on space between samples by collecting data in a different sequence. The data can be collected by electronically sequencing through the elements, eliminating the need for mechanically scanning the transducer. Removing the necessity for mechanical scanning can speed up the data collection.

In medical imaging, much research is being done to move to higher and higher frequencies, currently up to 100 MHz for opthalmic and dermatologic applications. To create an array of small high frequency sources, it would be necessary for each element to be on the order of 10 μm. Rather than making elements this small, an array of larger focused elements can be created.

Since virtual sources have been shown to behave the same as actual elements, designers of imaging systems have more freedom to choose the mode of imaging and processing that is applicable.

REFERENCES

[1] K. K. Shung, M. B. Smith, and B. Tsui, *Principles of Medical Imaging.* Toronto: Academic Press, Inc., 1992.

[2] M. O'Donnell and L. J. Thomas, "Efficient synthetic aperture imaging from a circular aperture with possible application to catheter-based imaging," *IEEE Trans. Ultrason., Ferroelect., Freq. Cont.*, vol. 39, no. 3, pp. 366–380, May 1992.

[3] C. Passman and H. Ermert, "Adaptive 150 MHz ultrasound imaging of the skin and the eye using an optimal combination of short pulse mode and pulse compression mode," *IEEE 1995 Ultrason. Symp. Proc*, vol. 2, Nov. 1995, pp. 1291–1294.

[4] S. G. Ye, K. A. Harasiewicz, C. J. Pavlin, and F. S. Foster, "Ultrasound characterization of normal ocular tissue in the frequency range from 50 MHz to 100 MHz," *IEEE Trans. Ultrason., Ferroelect., Freq. Cont.*, vol. 42, no. 1, pp. 8–14, Jan. 1995.

[5] A. J. Witten and W. C. King, "Acoustical imaging of subsurface features," *ASCE J. Envir. Engrg.*, vol. 116, pp. 166–181, 1990.

[6] C. B. Burckhardt, P. A. Grandchamp, and H. Hoffmann, "An experimental 2 MHz synthetic aperture sonar system intended for medical use," *IEEE Trans. Sonics Ultrason.*, vol. SU-21, no. 1, pp. 1–6, Jan. 1974.

[7] M. Karaman, P.-C. Li, and M. O'Donnell, "Synthetic aperture imaging for small scale systems," *IEEE Trans. Ultrason., Ferroelect., Freq. Cont.*, vol. 42, no. 3, pp. 429–442, May 1995.

[8] D. C. Munson, Jr., and R. L. Visentin, "A signal processing view of strip-mapping synthetic aperture radar," *IEEE Trans. Acoust., Speech, Signal Processing*, vol. 37, no. 12, pp. 2131–2147, Dec. 1989.

[9] J. Ylitalo, E. Alasaarela, and J. Koivukangas, "Ultrasound holographic B-scan imaging," *IEEE Trans. Ultrason., Ferroelect., Freq. Cont.*, vol. 36, no. 3, pp. 376–383, May 1989.

[10] M. O'Donnell, B. M. Shapo, M. J. Eberle, and D. N. Stephens, "Experimental studies on an efficient catheter array imaging system," *Ultrasonic Imaging*, vol. 17, pp. 83–94, 1995.

[11] J. T. Ylitalo and H. Ermert, "Ultrasound synthetic aperture imaging: Monostatic approach," *IEEE Trans. Ultrason., Ferroelect., Freq. Cont.*, vol. 41, no. 3, pp. 333–339, May 1994.

[12] C. Passman and H. Ermert, "In vivo imaging of the skin in the 100 MHz region using the synthetic aperture concept," *IEEE 1995 Ultrason. Symp. Proc.*, vol. 2, Nov. 1995, pp. 1287–1290.

[13] D. K. Peterson and G. S. Kino, "Real-time digital image reconstruction: A description of imaging hardware and an analysis of quantization errors," *IEEE Trans. Sonics Ultrason.*, vol. SU-31, no. 4, pp. 337–351, July 1984.

[14] B. D. Steinberg, "Digital beamforming in ultrasound," *IEEE Trans. Ultrason., Ferroelect., Freq. Cont.*, vol. 39, no. 6, pp. 716–721, Nov. 1992.

[15] M. O'Donnell et al., "Real-time phased array imaging using digital beam forming and autonomous channel control," *IEEE 1990 Utrason. Symp. Proc.*, vol. 3, Nov. 1990, pp. 1499–1502.

[16] S. W. Flax and M. O'Donnell, "Phase-aberration correction using signals from point reflectors and diffuse scatterers: Basic principles," *IEEE Trans. Ultrason., Ferroelect., Freq. Cont.*, vol. 35, no. 6, pp. 758–767, Nov. 1988.

[17] G. E. Trahey, "Phase aberration measurement and correction in medical ultrasound," *IEEE Engineering in Medicine and Biology Society 11th Annual International Conference*, vol. 1, 1989, pp. 397–399.

[18] M. Karaman, A. Atalar, and H. Koymen, "Adaptive digital beamforming for phased array ultrasound imaging," *1991 Ultrasonics Symposium*, vol. 2, Dec. 1991, pp. 1207–1210.